Journal of Computational Physics 228 (2009) 4088–4117

Contents lists available at ScienceDirect

Journal of Computational Physics

journal homepage: www.elsevier.com/locate/jcp

An axisymmetric computational model of generalized hydrodynamic theory for rarefied multi-species gas flows

Jae Wan Ahn, Chongam Kim *

School of Mechanical and Aerospace Engineering, Seoul National University, Seoul 151-744, Republic of Korea

ARTICLE INFO

Article history:
Received 28 June 2008
Received in revised form 7 February 2009
Accepted 16 February 2009
Available online 6 March 2009

PACS:
47.45.Ab
47.11.Df
05.70.Ln
51.10.+y

Keywords:
Generalized hydrodynamic equation
Hypersonic rarefied flow computations
Computational fluid dynamics
Second law of thermodynamics
Nonequilibrium effect

ABSTRACT

On the basis of the Eu's generalized hydrodynamic (GH) theories for diatomic single species gas and monatomic multi-species gas, an axisymmetric GH computational model for multi-species gas containing monatomic and diatomic molecules is developed for the numerical simulation of hypersonic rarefied gas flows. The multi-species GH computational model includes monatomic and diatomic species of O_2, N_2, NO, O, N. The mass diffusion flux of the gas mixture is included in the GH constitutive relation. In addition, the physical relationship between the mass diffusion and heat fluxes is added to the evolution equation set. The multi-species GH theory includes the rotational nonequilibrium effect of diatomic molecules by introducing excess normal stress associated with the bulk viscosity.

An efficient multi-species GH numerical solver for axisymmetric rarefied flows is then developed by adopting various numerical techniques, such as an adequate nonlinear equation solver for the GH constitutive relation, an accurate flux splitting scheme, multi-grid convergence acceleration and slip-wall boundary conditions. For validation, the proposed computational model is applied to hypersonic rarefied flows over a space shuttle nose, a sphere and a reentry body as well as 1D shock structure. By comparing the results of the multi-species GH model with those of the Navier–Stokes equation and the DSMC, the accuracy and physical consistency of the GH computational model are critically examined.

1. Introduction

In recent past several decades, the study of nonlinear gas flows in rarefied condition has been treated as an important topic. It has been motivated by the needs of tools to efficiently predict aero-thermodynamic loads on vehicles operating in high altitude. From this point of view, the development of computational models to predict gas flows over a large portion of rarefied flow regime is important. The primary physical parameter characterizing the rarefied flow is the Knudsen number [1], which is not small in high altitude condition. Though the Navier–Stokes (N–S) theory is capable of treating flow phenomena in a small deviation from the local equilibrium condition, it is not known to remain valid in the flow regime of a relatively large Knudsen number [2,3].

Much effort has been put into the development of a computational model beyond the N–S equations. Numerical models to predict the rarefied flow can be classified into two categories: the 'full kinetic (or molecular dynamic) model' and the 'fluid dynamic model'. In the former category, the direct simulation Monte Carlo (DSMC) is the most successful and powerful method [4–6]. At least, in terms of accuracy, there seems to be no alternative yet which can provide better results than

* Corresponding author. Tel.: +82 2 880 1915; fax: +82 2 887 2662.
E-mail address: chongam@snu.ac.kr (C. Kim).

0021-9991/$ - see front matter © 2009 Elsevier Inc. All rights reserved.
doi:10.1016/j.jcp.2009.02.026

DSMC. However, computational load of DSMC is very costly in comparison with fluid dynamic model, particularly in the regime near continuum limit [7]. Moreover, much experience is required to properly operate many tunable parameters.

On the other hand, fluid dynamic model is more attractive in terms of computational time cost and mathematical modelling. They can be formulated by hyperbolic conservation laws and some additional nonconserved variables. The nonconserved variables, such as the stress, the excess normal stress, the heat flux and the diffusion flux, are determined by the evolution equations which are derived with the help of the Boltzmann equation [2,8]. So far, several fluid dynamic models have been developed, such as the Bahtnagar–Gross–Krook (BGK) method [9,10], Burnett-type equations [11] and the Grad's moment method [2]. BGK method models the molecular collision term of the Boltzmann equation through the evolution process from the initial nonequilibrium to the final equilibrium state over the relaxation time scale. Various computational investigations based on the BGK theories have been carried out [9,10]. Some computations based on the Burnett-type equations, however, have shown several difficulties, such as numerical instability, violation of the second law of thermodynamics and the treatment of boundary condition. While the Maxwell–Grad moment method satisfies the second law of thermodynamics in the near equilibrium condition, it is not assured whether it is also valid in the condition far from the equilibrium [2].

Because physical consistency is as much important as computational efficiency, it is desirable to derive a fluid dynamic model for rarefied gas flows under the constraint of the fundamental physical laws, such as the second law of thermodynamics.

The generalized hydrodynamic (GH) theory developed by Eu [2,8,12–14] is derived under the strict constraint of the second law of thermodynamics. With the help of modern CFD techniques, there have been some effort and progress to establish a GH computational model for a single species gas in two-dimensional setting [7,15]. However, the axisymmetric extension of the diatomic GH model and the development of the multi-species GH model are prerequisite for realistic rarefied flow simulations. In addition, the effects of chemical reaction and the heterogeneous collision between monatomic and diatomic molecules have to be included for an accurate numerical modeling. Thus, the setup of the GH constitutive relations including heterogeneous molecular composition of species is essential.

Keeping these in mind, the GH computational model for multi-species gas including monatomic and diatomic molecules is developed, and it is extended into an axisymmetric formulation in the present work. By combining the monatomic multi-species [2] and diatomic single species GH models [8,7,16], the multi-species GH constitutive relations are formulated. The multi-species GH model takes into account the mass diffusion owing to molecular collision and thermal interaction. The excess normal stress is considered to represent the rotational energy of diatomic molecules.

To assess the reliability of the model and the accuracy of computational approximation, the proposed multi-species GH computational method is applied to the hypersonic rarefied flows over an axisymmetric shuttle nose, a sphere and a reentry body as well as 1D shock structure. The computed results are critically compared with the N–S and DSMC data.

2. Generalized hydrodynamic theory

Fluid dynamic approaches to compute rarefied flows generally start from the Boltzmann equation [2,17]. The formulation of the nonequilibrium distribution function to treat the collision term of the Boltzmann equation provides the foundation of each fluid dynamic theory, such as the BGK method [9], the Burnett equations [11] and the Grad's moment method [2]. In formulating those nonequilibrium distribution functions, there is no explicit constraint on the second law of thermodynamics [2,15], which indicates that some of the methods may not guarantee the positive entropy production.

On the other hand, the GH theory is derived under the strict constraint of the second law of thermodynamics. The nonequilibrium distribution function in the GH theory is defined as the following exponential form [2,12]:

$$f = \exp\left[-\frac{1}{k_B T}\left(\frac{1}{2}mc^2 + H_{rot} + \sum_{\alpha \geqslant 1} X^{(\alpha)} \odot h^{(\alpha)} - \mu_0\right)\right]. \tag{1}$$

A detailed explanation for Eq. (1) will be given later. Following the above definition of the nonequilibrium distribution function, the entropy production can be expressed as

$$\sigma_{ent} = k_B \kappa \sinh \kappa, \tag{2}$$

where k_B is the Boltzmann constant, and κ is the first-order cumulant introduced in deriving the entropy production. The detailed derivation of the entropy production can be found in the Ref. [2].

From Eq. (2), it is clear the entropy production is positive-definite, because κ is proportional to the square root of squared nonconserved variables (κ will be explained in the later part of this paper). This means that the GH theory always satisfies the second law of thermodynamics.

The primary difference between the GH model and the N–S model lies in the level of realizing the nonequilibrium effects in rarefied flow. In rarefied flow, the frequency of molecular collision is substantially reduced, and molecules need a longer time to reach the equilibrium state. The Navier–Stokes equations, on the contrary, assume the 'locally thermal equilibrium', which indicates that the gas model would take a shorter time to reach the equilibrium state. Even for high Knudsen number, the Navier–Stokes equations produce too much stress and heat flux (or too much momentum and energy exchange between

molecules), which is clearly contrary to the physics of rarefied flow. As quantitatively compared in Section 4, the stress and heat flux distributions provided by the GH model are asymptotically finite.

2.1. Derivation of the multi-species GH equations

By properly combining the GH theories for single species diatomic gas and monatomic gas mixtures [2,8], the general multi-species GH theory for heterogeneous gas including both monatomic and diatomic molecules can be derived.

The derivation process of the multi-species GH theory starts from the definition of the nonconserved variables ($\Phi_i^{(\alpha)}$) in terms of the nonequilibrium distribution function (f_i) and the molecular expressions (h_i^{α}) [2,12]. From now on, subscript i or j indicates the ith or jth species unless mentioned otherwise:

$$\Phi_i^{(\alpha)} = \langle h_i^{(\alpha)} f_i(\mathbf{v}, \mathbf{r}, t) \rangle. \tag{3}$$

Here, $\langle A \rangle$ indicates the mean value of A over particle velocity space

$$\langle A \rangle = \int A(\mathbf{v}_i) f_i(\mathbf{v}, \mathbf{r}, t) d\mathbf{v}.$$

In Eq. (3), $h_i^{(\alpha)}$ are defined as

$$\begin{aligned} h_i^{(1)} &= [m_i c_i c_i]^{(2)}, \\ h_i^{(2)} &= \frac{1}{3} m_i c_i^2 - \frac{p_i}{n_i}, \\ h_i^{(3)} &= \left(\frac{1}{2} m_i c_i^2 + m_i \psi_i - C_{p,i} T m_i \right) c_i, \\ h_i^{(4)} &= m_i c_i, \end{aligned} \tag{4}$$

where m_i, p_i and n_i represents the molecular mass, the partial pressure and the number density of the ith species in gas mixture, respectively. $C_{p,i}$ is the specific heat of the ith species per mass at constant pressure. $[A]^{(2)}$ is defined by

$$[A]^{(2)} = \frac{1}{2}(\mathbf{A} + \mathbf{A}^t) - \frac{1}{3} Tr(\mathbf{A}) \mathbf{I},$$

where $Tr(\mathbf{A})$ is the trace part of matrix $\mathbf{A}$, and $\mathbf{I}$ is the unit matrix.

With the definitions in Eq. (4), the nonconserved variables can be expressed as

$$\begin{aligned} &\Phi_i^{(1)} = \mathbf{\Pi}_i, \quad \Phi_i^{(2)} = \Delta_i, \\ &\Phi_i^{(3)} = \mathbf{Q}_i' = \mathbf{Q}_i - C_{p,i} T \mathbf{J}_i, \quad \Phi_i^{(4)} = \mathbf{J}_i. \end{aligned} \tag{5}$$

In the above relations, $\mathbf{\Pi}_i$, Δ_i, $\mathbf{Q}_i'$, $\mathbf{Q}_i$ and $\mathbf{J}_i$ represents the stress tensor, the excess normal stress, the heat flux vector, the total heat flux including diffusion effect and the diffusion flux, respectively. In the GH theory, the stress tensor $\mathbf{P}$ is decomposed into hydrostatic pressure p, stress $\mathbf{\Pi}$ and the excess normal stress Δ:

$$\mathbf{P} = p\mathbf{I} + \mathbf{\Pi} + \Delta \mathbf{I}.$$

The excess normal stress is related to the bulk viscosity and vanishes for monatomic molecules [2].

Inserting Eqs. (3)–(5) into the Boltzmann–Curtiss equation, the evolution equations of the nonconserved variables can be obtained [16,18]. The Boltzmann–Curtiss equation is expressed as

$$\left(\frac{\partial}{\partial t} + \mathbf{v} \cdot \nabla + \frac{\hat{j}_i}{I_i} \frac{\partial}{\partial \gamma_e} \right) f_i(\mathbf{v}, \mathbf{r}, \mathbf{j}, \gamma_e, t) = R[f], \tag{6}$$

where $\mathbf{j}$ and $\hat{j}$ denotes the angular momentum vector of diatomic species and its magnitude, respectively. γ_e is the azimuth Euler angle and $R[f]$ is the collision integral. As mentioned previously, the nonequilibrium distribution function of the ith species can be defined in the following exponential form:

$$f_i = \exp\left[-\frac{1}{k_B T} \left(\frac{1}{2} m_i c_i^2 + H_{rot} + \sum_{\alpha \geqslant 1} X_i^{(\alpha)} \odot h_i^{(\alpha)} - \mu_{0,i} \right) \right], \tag{7}$$

where $\mu_{0,i}$ is the normalization factor. The symbol $\odot$ denotes the scalar product of tensors $X_i^{(\alpha)}$ and $h_i^{(\alpha)}$. H_{rot} is the rotational Hamiltonian of diatomic species, which is defined as

$$H_{rot} = \frac{\mathbf{J} \cdot \mathbf{J}}{2I}. \tag{8}$$

Here, I is the moment of inertia of a diatomic molecule.

In Eq. (7), $X_i^{(\alpha)}$ can be treated as the function of macroscopic variables, such as density (ρ_i), flow velocity($\mathbf{u}$) and total energy(E):

$$X_i^{(\alpha)} = -\Phi_i^{(\alpha)} g_i^{(\alpha)}, \tag{9}$$

where $g_i^{(\alpha)}$ can be approximated as follows [2,12]:

$$g_i^{(1)} \simeq \frac{1}{2p_i}, \quad g_i^{(2)} \simeq \frac{3}{2p_i}, \quad g_i^{(3)} \simeq \frac{1}{p_i C_{p,i} T}, \quad g_i^{(4)} \simeq \frac{1}{\rho_i}. \tag{10}$$

With the definitions in Eqs. (4), (5) and (7), the Boltzmann–Curtiss equation provides the general form of the evolution equations as

$$\rho \frac{d}{dt}\left(\frac{\Phi_i^{(\alpha)}}{\rho}\right) = -\nabla \cdot \psi_i^{(\alpha)} + Z_i^{(\alpha)} + \Lambda_i^{(\alpha)}, \tag{11}$$

where $\nabla \cdot \psi_i^{(\alpha)}$ represent the fluxes of $h_i^{(\alpha)}$, which are mathematically one-order-higher than $\Phi_i^{(\alpha)}$. In general, these terms are reducible moments and can be set equal to zero [2,12].

In Eq. (11), the $Z_i^{(\alpha)}$ can be described as follows:

$$\begin{aligned}
Z_i^{(1)} &= -2(p_i + \omega\Delta_i)[\nabla u]^{(2)} - 2[\mathbf{J}_i d_t \mathbf{u}]^{(2)} - 2[\mathbf{\Pi}_i \cdot \nabla u]^{(2)},\\
Z_i^{(2)} &= -\frac{2}{3}\omega\left[d_t\mathbf{u}\cdot\mathbf{J}_i + \gamma'(\Delta_i\mathbf{I} + \mathbf{\Pi}_i) : \nabla u + \frac{3}{2}\mathbf{J}_i \cdot \nabla\left(\frac{p_i}{\rho_i}\right)\right],\\
Z_i^{(3)} &= -C_{p,i}T(p_i + \omega\Delta_i)\nabla \ln T - d_t\mathbf{u}\cdot(\mathbf{\Pi}_i + \omega\Delta_i\mathbf{I}) - \mathbf{Q}_i'\cdot\nabla u - \mathbf{\Pi}_i\cdot C_{p,i}\nabla T,\\
Z_i^{(4)} &= \nabla\cdot(p_i\mathbf{I} + \omega\Delta_i\mathbf{I} + \mathbf{\Pi}_i) + \frac{\rho_i}{\rho}\nabla\cdot\left(\mathbf{\Pi} + \sum_j(\omega\Delta_j)\mathbf{I}\right) - \nabla\cdot(\mathbf{\Pi}_i + \omega\Delta_i\mathbf{I}) - \mathbf{J}_i\cdot\nabla u - p\mathbf{d}_i.
\end{aligned} \tag{12}$$

Here, d_t means the material derivative, and $\mathbf{A}$:$\mathbf{B}$ indicates the double scalar product or $A_{ij}B_{ij}$ in tensorial notation. $\gamma' = (5-3\gamma)/2$ with the specific heat ratio of γ, and $\mathbf{Q}_i' = \mathbf{Q}_i - C_{p,i}T\mathbf{J}_i$ is the heat flux vector without diffusion effect. In the fourth relation, $\mathbf{d}_i = \nabla(n_i/n)$. The parameter ω is 1 for diatomic species and 0 for monatomic species.

Eq. (11) is the universal evolution equation for the fluid dynamic methods, and it does not have any special approximation [2,12]. The difference of the GH equations from other fluid dynamic models lies in the definition of the dissipation terms or $\Lambda_i^{(\alpha)}$.

The dissipation terms of the GH equations are defined as the following relations:

$$\mathbf{\Lambda}_i^{(1)} = -2p_i q(\kappa)\sum_{j=1}^{r}\mathfrak{R}_{ij}^{(11)}\mathbf{\Pi}_j, \tag{13}$$

$$\mathbf{\Lambda}_i^{(2)} = -\frac{2}{3}p_i q(\kappa)\sum_{j=1}^{r}\mathfrak{R}_{ij}^{(22)}\Delta_j, \tag{14}$$

$$\mathbf{\Lambda}_i^{(3)} = -p_i C_{p,i} T q(\kappa)\sum_{j=1}^{r}\left(\mathfrak{R}_{ij}^{(33)}\mathbf{Q}_j' + \mathfrak{R}_{ij}^{(34)}\frac{\mathbf{J}_j}{\rho_j}\right), \tag{15}$$

$$\mathbf{\Lambda}_i^{(4)} = -q(\kappa)\sum_{j=1}^{r}\left(\mathfrak{R}_{ij}^{(43)}\mathbf{Q}_j' + \mathfrak{R}_{ij}^{(44)}\frac{\mathbf{J}_j}{\rho_j}\right), \tag{16}$$

where

$$q(\kappa) = \frac{\sinh\kappa}{\kappa}. \tag{17}$$

κ can be derived by using the cumulant approximation, and it is expressed as

$$\kappa^2 = \frac{g}{k_B T}\sum_{i,j=1}^{r}\left[\mathfrak{R}_{ij}^{(11)}\mathbf{\Pi}_i : \mathbf{\Pi}_j + \mathfrak{R}_{ij}^{(22)}\Delta_i\Delta_j + \mathbf{Q}_i'\cdot\left(\mathfrak{R}_{ij}^{(33)}\mathbf{Q}_j' + \mathfrak{R}_{ij}^{(34)}\frac{\mathbf{J}_j}{\rho_j}\right) + \frac{\mathbf{J}_i}{\rho_i}\cdot\left(\mathfrak{R}_{ij}^{(43)}\mathbf{Q}_j' + \mathfrak{R}_{ij}^{(44)}\frac{\mathbf{J}_j}{\rho_j}\right)\right], \tag{18}$$

where g is the relative velocity of molecules defined as

$$g = \frac{1}{n^2 d^2}\sqrt{\frac{m}{2k_B T}}, \tag{19}$$

and r indicates the number of species.

Unlike $Z_i^{(\alpha)}$ of Eq. (12), $\Lambda_i^{(\alpha)}$ and κ of Eqs. (13)–(18) contain $\mathfrak{R}_{ij}^{(\alpha\beta)}$. $\mathfrak{R}_{ij}^{(\alpha\beta)}$ are related to the collision integrals $R[f]$ between various species, which can be defined by $\mathfrak{R}_{ij}^{(\alpha\beta)} = \frac{g}{k_B T} g_i^{(\alpha)} R_{ij}^{(\alpha\beta)} g_j^{(\beta)}$. $R_{ij}^{(\alpha\beta)}$ are the collision bracket integrals and can be determined

by molecular properties such as molecular mass, random velocity and so on. As shown in Table 3.2 of Ref. [12], the mathematical process to completely determine $R_{ij}^{(\alpha\beta)}$ is too complicated. For an efficient computational implementation without compromising the essence of the collision bracket integrals, the following simple formulation is used [12]:

$$-2[\nabla u]^{(2)} = q(\kappa)\sum_{j=1}^{r}\mathfrak{R}_{ij}^{(11)}\mathbf{\Pi}_j, \tag{20}$$

$$-\gamma'\nabla\cdot\mathbf{u} = q(\kappa)\sum_{j=1}^{r}\mathfrak{R}_{ij}^{(22)}\Delta_j, \tag{21}$$

$$-\nabla\ln T = q(\kappa)\sum_{j=1}^{r}\left(\mathfrak{R}_{ij}^{(33)}\mathbf{Q}_j' + \mathfrak{R}_{ij}^{(34)}\frac{\mathbf{J}_j}{\rho_j}\right), \tag{22}$$

$$-\frac{p}{\rho_i}\mathbf{d}_i = q(\kappa)\sum_{j=1}^{r}\left(\mathfrak{R}_{ij}^{(43)}\mathbf{Q}_j' + \mathfrak{R}_{ij}^{(44)}\frac{\mathbf{J}_j}{\rho_j}\right). \tag{23}$$

According to Eu's works [2,8,12–14], Eqs. (20)–(23) are still reliable in large Knudsen number flows. Thus, they can be used to obtain $\Delta_i^{(\alpha)}$ without the detailed determination of the collision integrals $R_{ij}^{(\alpha\beta)}$, which eventually leads to the proper constitutive relations for the multi-species GH computational model.

2.2. Determination of $\Delta_i^{(\alpha)}$

In order to obtain $\Delta_i^{(\alpha)}$ without $\mathfrak{R}_{ij}^{(\alpha\beta)}$, Eqs. (13)–(16) are firstly converted into the following matrix equations:

$$\mathbf{\Lambda}^{(1)} = -q(\kappa)\mathbf{S}\mathbf{\Pi}_\mathbf{s}, \tag{24}$$

$$\mathbf{\Lambda}^{(2)} = -q(\kappa)\mathbf{R}\mathbf{\Delta}_\mathbf{s}, \tag{25}$$

$$\mathbf{\Lambda}^{(3,4)} = -q(\kappa)\mathbf{M}\mathbf{Q}_\mathbf{s}, \tag{26}$$

where bold characters are defined as follows:

$$\mathbf{\Lambda}^{(1)} = \begin{pmatrix} \frac{\Lambda_1^{(1)}}{2p_1} \\ \vdots \\ \frac{\Lambda_r^{(1)}}{2p_r} \end{pmatrix}, \quad \mathbf{S} = \begin{pmatrix} \mathfrak{R}_{11}^{(11)} & \cdots & \mathfrak{R}_{1r}^{(11)} \\ \vdots & \ddots & \vdots \\ \mathfrak{R}_{r1}^{(11)} & \cdots & \mathfrak{R}_{rr}^{(11)} \end{pmatrix}, \quad \mathbf{\Pi}_\mathbf{s} = \begin{pmatrix} \mathbf{\Pi}_1 \\ \vdots \\ \mathbf{\Pi}_\mathbf{r} \end{pmatrix},$$

$$\mathbf{\Lambda}^{(2)} = \begin{pmatrix} \frac{3\Delta_1^{(2)}}{2p_1} \\ \vdots \\ \frac{3\Delta_r^{(2)}}{2p_r} \end{pmatrix}, \quad \mathbf{R} = \begin{pmatrix} \mathfrak{R}_{11}^{(22)} & \cdots & \mathfrak{R}_{1r}^{(22)} \\ \vdots & \ddots & \vdots \\ \mathfrak{R}_{r1}^{(22)} & \cdots & \mathfrak{R}_{rr}^{(22)} \end{pmatrix}, \quad \mathbf{\Delta}_\mathbf{s} = \begin{pmatrix} \Delta_1 \\ \vdots \\ \Delta_r \end{pmatrix},$$

$$\mathbf{\Lambda}^{(3,4)} = \begin{pmatrix} \frac{\Lambda_1^{(3)}}{p_1 C_{p,1} T} \\ \vdots \\ \frac{\Lambda_r^{(3)}}{p_r C_{p,r} T} \\ \Lambda_1^{(4)} \\ \vdots \\ \Lambda_r^{(4)} \end{pmatrix}, \quad \mathbf{M} = \begin{pmatrix} \mathfrak{R}_{11}^{(33)} & \cdots & \mathfrak{R}_{1r}^{(33)} & \mathfrak{R}_{11}^{(34)} & \cdots & \mathfrak{R}_{1r}^{(34)} \\ \vdots & \ddots & \vdots & \vdots & \ddots & \vdots \\ \mathfrak{R}_{r1}^{(33)} & \cdots & \mathfrak{R}_{rr}^{(33)} & \mathfrak{R}_{r1}^{(34)} & \cdots & \mathfrak{R}_{rr}^{(34)} \\ \mathfrak{R}_{11}^{(43)} & \cdots & \mathfrak{R}_{1r}^{(43)} & \mathfrak{R}_{11}^{(44)} & \cdots & Re_{1r}^{(44)} \\ \vdots & \ddots & \vdots & \vdots & \ddots & \vdots \\ \mathfrak{R}_{r1}^{(43)} & \cdots & \mathfrak{R}_{rr}^{(43)} & \mathfrak{R}_{r1}^{(44)} & \cdots & \mathfrak{R}_{rr}^{(44)} \end{pmatrix}, \quad \mathbf{Q}_\mathbf{s} = \begin{pmatrix} \mathbf{Q}_1' \\ \vdots \\ \mathbf{Q}_r' \\ \frac{\mathbf{J}_1}{\rho_1} \\ \vdots \\ \frac{\mathbf{J}_r}{\rho_r} \end{pmatrix}.$$

Then, Eqs. (20)–(23) can then be expressed as follows:

$$q(\kappa)\sum_{i=1}^{r}\mathbf{\Pi}_i = -2[\nabla u]^{(2)}\sum_{i,j=1}^{r}(\mathbf{S}^{-1})_{ij}, \tag{27}$$

$$q(\kappa)\sum_{i=1}^{r}\Delta_i = -\nabla\cdot\mathbf{u}\sum_{i,j=1}^{r}(\mathbf{R}^{-1})_{ij}, \tag{28}$$

$$q(\kappa)\sum_{i=1}^{r}\mathbf{Q}_i' = -\nabla\ln T\sum_{i,j=1}^{r}(\mathbf{M}^{-1})_{ij}^{(33)} - \sum_{i,j=1}^{r}(\mathbf{M}^{-1})_{ij}^{(34)}\frac{p}{\rho_i}\mathbf{d}_i, \tag{29}$$

$$q(\kappa)\sum_{i=1}^{r}\frac{\mathbf{J}_i}{\rho_i} = -\nabla\ln T\sum_{i,j=1}^{r}(\mathbf{M}^{-1})_{ij}^{(43)} - \sum_{i,j=1}^{r}(\mathbf{M}^{-1})_{ij}^{(44)}\frac{p}{\rho_i}\mathbf{d}_i. \tag{30}$$

Here, the relations of the first-order Chapman–Enskog transport coefficients are introduced [12]:

$$\mu_0 = \sum_{i,j=1}^{r} (\mathbf{S}^{-1})_{ij}, \quad \mu_{b,0} = \sum_{i,j=1}^{r} (\mathbf{R}^{-1})_{ij}, \tag{31}$$

$$\lambda_0 = \sum_{i,j=1}^{r} (\mathbf{M}^{-1})_{ij}^{(33)}, \tag{32}$$

$$D_{T,i}^0 = \sum_{j=1}^{r} \frac{1}{\rho_j} (\mathbf{M}^{-1})_{ij}^{(34)}, \quad D_{ij}^0 = \frac{p}{\rho_j} (\mathbf{M}^{-1})_{ij}^{(44)}, \tag{33}$$

where μ_b is the bulk viscosity, and λ denotes the heat conductivity multiplied by temperature ($\lambda = kT$). D_{ij} and $D_{T,i}$ represents the diffusion and the thermal diffusion coefficient, respectively.

By using Eqs. (31)–(33) and the symmetry of $\mathfrak{R}_{ij}^{(\alpha\beta)} = \mathfrak{R}_{ij}^{(\beta\alpha)}$ (or equivalently, the symmetry of $(\mathbf{M}^{-1})_{ij}^{(43)} = (\mathbf{M}^{-1})_{ij}^{(34)}$), Eqs. (27)–(30) can be expressed in terms of the first-order Chapman–Enskog transport coefficients:

$$q(\kappa) \sum_{i=1}^{r} \mathbf{\Pi}_i = -2\mu_0 [\nabla u]^{(2)}, \tag{34}$$

$$q(\kappa) \sum_{i=1}^{r} \Delta_i = -\mu_{b,0} \nabla \cdot \mathbf{u}, \tag{35}$$

$$q(\kappa) \sum_{i=1}^{r} \mathbf{Q}_i' = -\lambda_0 \nabla \ln T - p \sum_{i=1}^{r} D_{T,i}^0 \mathbf{d}_i, \tag{36}$$

$$q(\kappa) \sum_{i=1}^{r} \frac{\mathbf{J}_i}{\rho_i} = -\sum_{i=1}^{r} D_{T,i}^0 \rho_i \nabla \ln T - \sum_{i,j=1}^{r} D_{ij}^0 \mathbf{d}_i. \tag{37}$$

From Eqs. (34)–(37), the proper relations for the right hand side of Eqs. (20)–(23) are obtained as follows:

$$[\nabla u]^{(2)} = -\frac{1}{2\mu_0} q(\kappa) \sum_{i=1}^{r} \mathbf{\Pi}_i, \tag{38}$$

$$\nabla \cdot \mathbf{u} = -\frac{1}{\mu_{b,0}} q(\kappa) \sum_{i=1}^{r} \Delta_i, \tag{39}$$

$$\nabla \ln T = -\frac{1}{\lambda_0} q(\kappa) \sum_{i=1}^{r} \mathbf{Q}_i', \tag{40}$$

$$\frac{p}{\rho_i} \mathbf{d}_i = -pq(\kappa) \left[(\mathbf{D}^{-1})_i \frac{\mathbf{J}_i}{\rho_i} - \frac{k_{T,i}}{\lambda_0} \mathbf{Q}_i' \right], \tag{41}$$

where $\mathbf{D}$ is the matrix of the diffusion coefficients D_{ij}, and $k_{T,i}$ is the thermal diffusion ratio. The following relation is valid between the thermal diffusion and binary collision diffusion coefficients [17,12]:

$$D_{T,i} = \sum_{j=1}^{r} k_{T,j} D_{ij}. \tag{42}$$

In deriving Eqs. (38)–(41), it is assumed that the terms such as $\nabla \cdot \mathbf{u}$, $[\nabla u]^{(2)}$ and $\lambda_0 \nabla \ln T$ are global properties, and they do not explicitly depend on the species. For example, the stress of each species is defined as $\mathbf{\Pi}_i = \mu_i [\nabla u]^{(2)}$, not as $\mathbf{\Pi}_i = \mu_i [\nabla u_i]^{(2)}$, and the global stress becomes the sum of $\mathbf{\Pi}_i$ $\left(\text{i.e., } \mathbf{\Pi} = \sum_{i=1}^{r} \mathbf{\Pi}_i = -2\mu_0 [\nabla u]^{(2)} = -2\left(\sum_{i=1}^{r} \mu_i\right) [\nabla u]^{(2)} \right.$ and $\left.\sum_{i=1}^{r} \mu_i = \mu_0\right)$. The diffusion flux $\mathbf{J}_i$ consists of the binary collision diffusion and the thermal diffusion:

$$\frac{\mathbf{J}_i}{\rho_i} = \sum_{j=1}^{r} D_{ij} \mathbf{d}_i + D_{T,i} \nabla \ln T = \sum_{j=1}^{r} D_{ij} (\mathbf{d}_i + k_{T,j} \nabla \ln T). \tag{43}$$

By inserting Eqs. (38)–(41) into Eqs. (20)–(23) and Eqs. (13)–(16), the final formulation of $\Lambda_i^{(\alpha)}$ can be obtained:

$$\mathbf{\Lambda}_i^{(1)} = -2 \frac{p_i}{\mu_0} q(\kappa) \sum_{i=1}^{r} \mathbf{\Pi}_i, \tag{44}$$

$$\mathbf{\Lambda}_i^{(2)} = -\frac{2}{3} \frac{\gamma' p_i}{\mu_{b,0}} q(\kappa) \sum_{i=1}^{r} \Delta_i, \tag{45}$$

$$\mathbf{\Lambda}_i^{(3)} = -\frac{p_i C_{p,i} T}{\lambda_0} q(\kappa) \sum_{i=1}^{r} \mathbf{Q}_i', \tag{46}$$

$$\mathbf{\Lambda}_i^{(4)} = -pq(\kappa) \left[(\mathbf{D}^{-1})_i \frac{\mathbf{J}_i}{\rho_i} - \frac{k_{T,i}}{\lambda_0} \mathbf{Q}_i' \right]. \tag{47}$$

The heterogeneous collision between monatomic and diatomic molecules is taken into account through the diffusion matrix in Eq. (47). Since only diatomic species can produce the excess normal stress, Δ_i is vanished for monatomic species. The parameter ω is introduced in Eq. (12) to check the excess normal stress. For monatomic species, the excess normal stress relation ($\Lambda_i^{(2)}$) and Δ_i are discarded by setting $\omega = 0$.

In the diffusion relations, the binary diffusion coefficient (D_{ij}) and the thermal diffusion ratio ($k_{T,i}$) corresponding to monatomic–monatomic, diatomic–diatomic and monatomic–diatomic collisions have to be distinguished. According to Ref. [17], they lie in the range of $D_{\text{monatomic–monatomic}} \cong 0.1$—$0.2$, $D_{\text{monatomic–diatomic}} \cong 0.4$—$0.5$ and $D_{\text{diatomic–diatomic}} \cong 0.6$—$0.8$. In this work, $D_{\text{monatomic–monatomic}} = 0.18$, $D_{\text{monatomic–diatomic}} = 0.48$ and $D_{\text{diatomic–diatomic}} = 0.65$. The thermal diffusion coefficient $k_{T,i}$ is defined as $k_{T,i} = \alpha(n_i/n)(n_j/n)$, where $\alpha \cong 0.02$ and (n_i/n) is the mole fraction of the ith species.

By using the relations of Eqs. (20)–(23) and Eqs. (38)–(41), κ (or Eq. (18)) can be converted into the following expression:

$$\kappa^2 = \frac{g}{k_B T}\sum_{i,j=1}^{r}\left[\frac{\mathbf{\Pi}_i : \mathbf{\Pi}_j}{\mu_0} + \gamma'\frac{\Delta_i\Delta_j}{\mu_{b,0}} + \frac{\mathbf{Q}_i'\cdot\mathbf{Q}_j'}{\lambda_0} + pD_{ij}\mathbf{d}_i\cdot\mathbf{d}_j\right]. \tag{48}$$

In summary, two key-ingredients for the computations of the multi-species GH equations are examined in this section: one is the determination of dissipation terms $\Lambda_i^{(\alpha)}$ in an explicit from of conserved and nonconserved variables, and the other is the appropriate treatment of heterogeneous molecular collisions.

2.3. The constitutive relations of the multi-species GH theory

The constitutive relations of the multi-species GH theory can be obtained by inserting Eq. (12) and Eqs. (44)–(47) into Eq. (11):

$$\rho\frac{d}{dt}\left(\frac{\mathbf{\Pi}_i}{\rho}\right) = -2(p_i+\omega\Delta_i)[\nabla u]^{(2)} - 2[\mathbf{J}_i d_t\mathbf{u}]^{(2)} - 2[\mathbf{\Pi}_i\cdot\nabla u]^{(2)} - \frac{p_i}{\mu}q(\kappa)\sum_{i=1}^{r}\mathbf{\Pi}_i, \tag{49}$$

$$\rho\frac{d}{dt}\left(\frac{\Delta_i}{\rho}\right) = -\omega\left[\frac{2}{3}d_t\mathbf{u}\cdot\mathbf{J}_i + \frac{2}{3}\gamma'(\Delta_i\mathbf{I}+\mathbf{\Pi}_i):\nabla u + \mathbf{J}_i\cdot\nabla\left(\frac{p_i}{\rho_i}\right) + \frac{2}{3}\gamma'\frac{p_i}{\mu_b}q(\kappa)\sum_{i=1}^{r}\Delta_i\right], \tag{50}$$

$$\rho\frac{d}{dt}\left(\frac{\mathbf{Q}_i'}{\rho}\right) = -C_{p,i}T(p_i+\omega\Delta_i)\nabla\ln T - d_t\mathbf{u}\cdot(\mathbf{\Pi}_i+\omega\Delta_i\mathbf{I}) - \mathbf{Q}_i'\cdot\nabla u - \mathbf{\Pi}_i\cdot C_{p,i}\nabla T - \frac{p_i C_{p,i}T}{\lambda}q(\kappa)\sum_{i=1}^{r}\mathbf{Q}_i', \tag{51}$$

$$\begin{aligned}\rho\frac{d}{dt}\left(\frac{\mathbf{J}_i}{\rho}\right) &= \nabla\cdot(p_i\mathbf{I}+\omega\Delta_i\mathbf{I}+\mathbf{\Pi}_i) + \frac{\rho_i}{\rho}\nabla\cdot\left(\mathbf{\Pi}_i + \sum_{j=1}^{r}(\omega\Delta_j)\mathbf{I}\right) - \nabla\cdot(\mathbf{\Pi}_i+\omega\Delta_i\mathbf{I}) - \mathbf{J}_i\cdot\nabla u - p\mathbf{d}_i \\ &\quad - pq(\kappa)\left[(\mathbf{D}^{-1})_i\frac{\mathbf{J}_i}{\rho_i} - \frac{k_{T,i}}{\lambda}\mathbf{Q}_i'\right].\end{aligned} \tag{52}$$

Eqs. (49)–(52) contain the cases of the single species GH theory for diatomic gas and the multi-species GH theory for monatomic gas. From $\sum_{i=1}^{r}\mathbf{\Pi}_i = \mathbf{\Pi}$, $\sum_{i=1}^{r}\Delta_i = \Delta$ and $\sum_{i=1}^{r}\mathbf{Q}_i' = \mathbf{Q}'$, and by ignoring the diffusion relations, they reduce to the GH constitutive relations for diatomic single species gases. Furthermore, if the excess normal stress for diatomic species is ignored (or $\omega = 0$), the GH constitutive relations for single species monatomic gases can be obtained.

Together with the constitutive relations, the following extended conservation laws become the axisymmetric governing equations for the multi-species GH theory:

$$\frac{\partial}{\partial t}\begin{pmatrix}\rho\\ \rho\mathbf{u}\\ \rho E\\ \rho_i\end{pmatrix} + \nabla\cdot\begin{pmatrix}\rho\mathbf{u}\\ \rho\mathbf{u}\mathbf{u}+p\mathbf{I}\\ (\rho E+p)\mathbf{u}\\ \rho_i\mathbf{u}\end{pmatrix} + \nabla\cdot\begin{pmatrix}0\\ \sum_{i=1}^{r}(\mathbf{\Pi}_i+\omega\Delta_i\mathbf{I})\\ \sum_{i=1}^{r}(\mathbf{\Pi}_i+\omega\Delta_i\mathbf{I})\cdot\mathbf{u}+\mathbf{Q}\\ \frac{\rho_i}{\rho}D_{c,i}c_{c,i}\end{pmatrix} + \frac{(\mathbf{H}+\mathbf{H}_v)}{y} = \begin{pmatrix}0\\0\\0\\S_i\end{pmatrix}, \tag{53}$$

where $\mathbf{H}$ and $\mathbf{H}_v$ is the inviscid and viscous axisymmetric source term, respectively, defined as in the N–S theory. The last line of Eq. (53) is the chemical species equation explained in Appendix A.

Although the derivation process of the GH governing equations is rather complicated, the mathematical form is quite similar to the conventional N–S equations except for the presence of the excess normal stress. The nonconserved variables, such as $\mathbf{\Pi}$, Δ, $\mathbf{Q}$ and $\mathbf{J}$, are determined from the GH constitutive relations.

The thermodynamic path of the GH theory is exact so long as no approximation is introduced in the derivation procedure. Firstly, the evolution equation in Eq. (11) including Eq. (12) is thermodynamically exact since there is no assumption. For f_i in Eq. (7) and $\Lambda_i^{(\alpha)}$, the thermodynamic path may depend on the definition of the term $X_i^{(\alpha)}$ in f_i and $\Lambda_i^{(\alpha)}$. Therefore, the GH theory is theoretically solid in its original form but, as in Eq. (9), some approximation at implementation step may not guarantee the exact thermodynamic path. From this perspective, we are going to examine the level of physical/numerical accuracy and robustness of the GH equations, which is seriously deteriorated in other continuum-based computational models such as Burnett-type equations. Considering the violation of the second law of thermodynamics of the Burnett equations, the GH

theory is physically much more preferable than the Burnett equations and the Navier–Stokes equation. In addition, it has been proved that the GH theory satisfies the H-theorem so that the final entropy production, unless the flow is isentropic, is always positive-definite [2,8,12].

3. Computational model for the multi-species GH theory

The constitutive relations of the multi-species GH theory are composed of a coupled set of nonlinear differential equations, and it is very costly to directly solve them. With a suitable physical assumption, however, they can be converted into a set of nonlinear algebraic equations. In this section, the computational procedure of the multi-species GH theory is described. In addition, the axisymmetric extension of the GH constitutive relations and the slip-wall boundary condition are explained.

3.1. The computational model of the GH constitutive relations

The left-hand-side of the constitutive GH relations (Eqs. (49)–(52)) is the time-derivative term of the nonconserved variables. The time scales to reach the equilibrium state between the conserved variables (ρ, $\mathbf{u}$ and E) and the nonconserved variables ($\mathbf{\Pi}$, Δ and $\mathbf{Q}$) are generally different depending on the order of gas particle moments [1]. According to Eu's adiabatic approximation [2], the nonconserved variables change much faster than the conserved variables and quickly reach to steady states. Thus, the time-derivative term can be neglected, and Eqs. (49)–(52) can be simplified into a set of nonlinear algebraic equations. For example, Eq. (49) becomes

$$\frac{p_i}{\mu} q(\kappa) \sum_{i=1}^{r} \mathbf{\Pi}_i = -2(p_i + \omega \Delta_i)[\nabla u]^{(2)} - 2[\mathbf{J}_i d_t \mathbf{u}]^{(2)} - 2[\mathbf{\Pi}_i \cdot \nabla u]^{(2)}. \tag{54}$$

After a suitable nondimensionalization, the dimensionless algebraic form of the constitutive relations can be obtained as follows:

$$q(\kappa) \sum_{j=1}^{r} \mathbf{\Pi}_j = \left(1 + \frac{\omega f_b}{Re\, p_i} \Delta_i\right) \mathbf{\Pi}_0 - \frac{2}{Re\, p_i} \frac{\mu}{S_c} [\mathbf{J}_i d_t \mathbf{u}]^{(2)} - \frac{2\mu}{Re\, p_i} [\mathbf{\Pi}_i \cdot \nabla u]^{(2)}, \tag{55}$$

$$q(\kappa) \sum_{j=1}^{r} \Delta_j = \Delta_0 - f_b \frac{\mu}{Re\, p_i} (\mathbf{\Pi}_i + f_b \Delta_i \mathbf{I}) : \nabla u - \frac{f_b}{\gamma'} \frac{\mu}{Re\, p_i} \frac{1}{S_c} \left[d_t \mathbf{u} \cdot \mathbf{J}_i + \mathbf{J}_i \cdot \nabla \left(\frac{p_i}{\rho_i} \right) \right], \tag{56}$$

$$q(\kappa) \sum_{j=1}^{r} \mathbf{Q}_i' = \left(1 + \frac{\omega f_b}{Re\, p_i} \Delta_i\right) \mathbf{Q}_0' - \frac{1}{Re\, p_i} \frac{\mu}{Pr} d_t \mathbf{u} \cdot (\mathbf{\Pi}_i + \omega f_b \Delta_i \mathbf{I}) - \frac{1}{Re\, p_i} \frac{\mu}{Pr} \mathbf{Q}_i' \cdot \nabla u + \frac{1}{Re\, p_i} \mathbf{\Pi}_i \cdot \mathbf{Q}_0', \tag{57}$$

$$\begin{aligned} q(\kappa) \left[(\mathbf{D}^{-1})_i \frac{\mathbf{J}_i}{\rho_i} - \frac{(\gamma - 1)\rho_0}{Pr} \mathbf{Q}_i' \right] &= \rho_0 \nabla \cdot \left(\frac{p_i}{p} \mathbf{I} + \frac{\omega f_b}{Re\, p} \Delta_i \mathbf{I} + \frac{1}{Re\, p} \mathbf{\Pi}_i \right) + \frac{\rho_0 \rho_i}{Re\, p} \nabla \cdot (\mathbf{\Pi} + \omega f_b \Delta \mathbf{I}) \\ &\quad - \frac{\rho_0}{Re\, p} \nabla \cdot (\mathbf{\Pi}_i + \omega f_b \Delta_i \mathbf{I}) - \frac{\rho_0}{Re\, p S_c} \mathbf{J}_i \cdot \nabla u - \mathbf{d}_i. \end{aligned} \tag{58}$$

And, the first-order cumulant κ in Eq. (48) becomes

$$\kappa^2 = \frac{c}{Re\, p} \sum_{i,j=1}^{r} \left[\mathbf{\Pi}_i : \mathbf{\Pi}_j + \omega \gamma' f_b \Delta_i \Delta_j + \frac{(\gamma - 1) Pr}{T} \mathbf{Q}_i' \cdot \mathbf{Q}_j' + \frac{D_{ij}}{\rho_0 S_c} \mathbf{d}_i \cdot \mathbf{d}_j \right], \tag{59}$$

where S_c and Pr is the Schimdt number and the Prandtl number, respectively.

In Eq. (59), $f_b = \mu_b/\mu$, and the constant c takes a value between 1.0138 (Maxwellian molecule) and 1.2232 ($\nu = 3$) [17]. ν is the exponent of the inverse power law for the gas particle interaction potential. The subscript 0 indicates the first-order approximation of the Chapman–Enskog expansion or the value obtained by the N–S theory. Thus, the stress and the heat flux by the N–S theory can be described as

$$\mathbf{\Pi}_0 = -2\mu[\nabla u]^{(2)}, \quad \Delta_0 = -\mu_b \nabla \cdot \mathbf{u}, \quad \mathbf{Q}_0 = -\lambda \nabla \ln T. \tag{60}$$

Eqs. (55)–(59) can be solved by a suitable numerical solver. In computation, the N–S stress and heat flux can be used as the initial conditions of the GH constitutive relations. Overall computational procedure will be explained in Section 4.

3.2. The axisymmetric GH constitutive relations

The axisymmetric GH computational model is obtained by decomposing $\mathbf{\Pi}$, $\mathbf{Q}$ and $\mathbf{J}$ into cylindrical coordinates, (r, θ, z) with the assumption that all components of the θ direction are zero, i.e., u_θ, $\frac{\partial}{\partial \theta}$, $Q_\theta' = 0$. Care must be taken that the $\theta\theta$ component of tensor, such as $\Pi_{\theta\theta}$, does not vanish since $\Pi_{\theta\theta} = -(\Pi_{zz} + \Pi_{rr})$. All components of the axisymmetric constitutive relations are listed in Appendix B.

3.3. Slip-wall boundary conditions

Appropriate slip-wall boundary conditions are crucial in rarefied flow computations because the velocity-slip and temperature-jump provide a significant impact on computational accuracy. Since rarefied gas molecules near wall boundary do not have enough collisions to reach the equilibrium state, the non-slip boundary condition is not consistent with the molecular physics. As a slip boundary condition, the Langmuir slip condition [21] and the Maxwell–Smoluchowski condition [25,26] are employed in the present work.

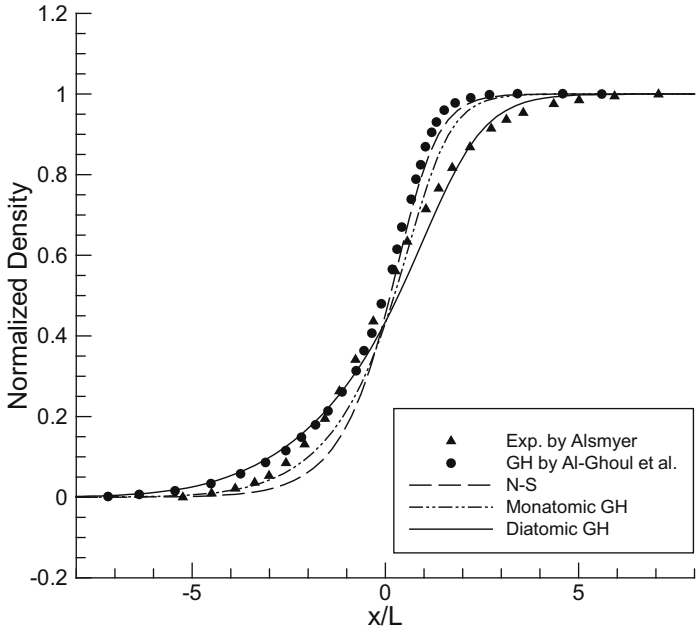

Fig. 1. Normalized density distribution for a diatomic gas($M = 2.0$). Experiment data are taken from Alsmyer's work [34] and diatomic GH result by Al-Goul et al. [37] is also depicted.

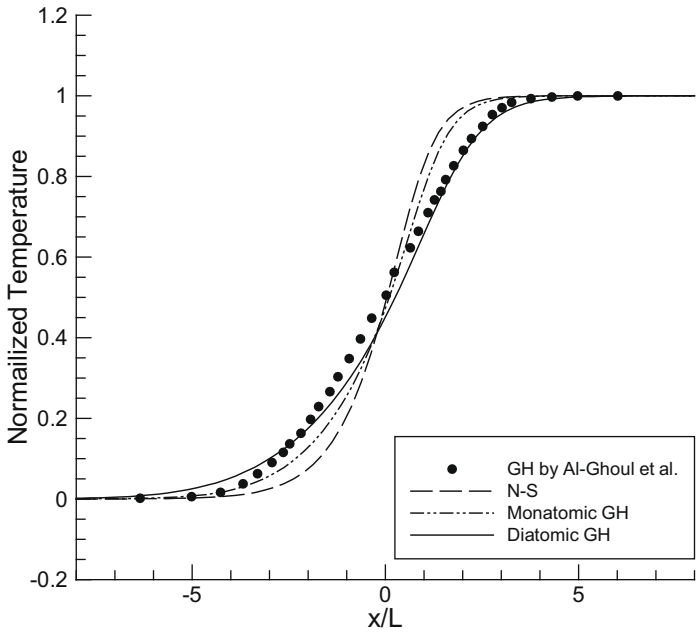

Fig. 2. Normalized temperature distribution for a diatomic gas ($M = 2.0$). Diatomic GH result by Al-Goul et al. [37] is also depicted.

The Langmuir boundary condition can be expressed as

$$u_s = \alpha u_w + (1-\alpha)u_g, \quad T_s = \alpha T_w + (1-\alpha)T_g, \tag{61}$$

where the subscript s represents slip quantity, w stands for the wall and g denotes the local gas flow value adjacent to the wall. The parameter α plays a role of determining the portion of wall and gas characteristics, which can be described as [22–24]

$$\alpha = n_{N_2}\frac{\sqrt{\beta_{N_2}p}}{1+\sqrt{\beta_{N_2}p}} + n_{O_2}\frac{\sqrt{\beta_{N_2}p}}{1+\sqrt{\beta_{N_2}p}}, \tag{62}$$

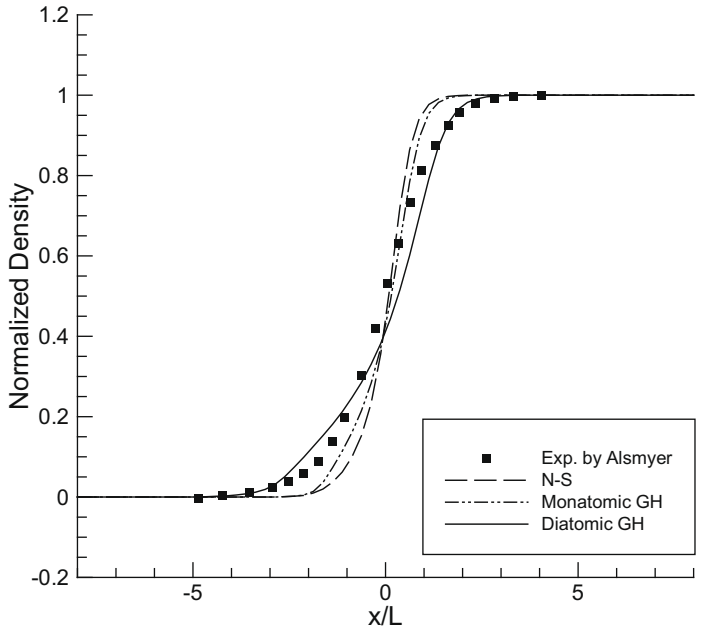

Fig. 3. Normalized density distribution for a diatomic gas($M = 6.1$). Experiment data are taken from Alsmyer's work [34].

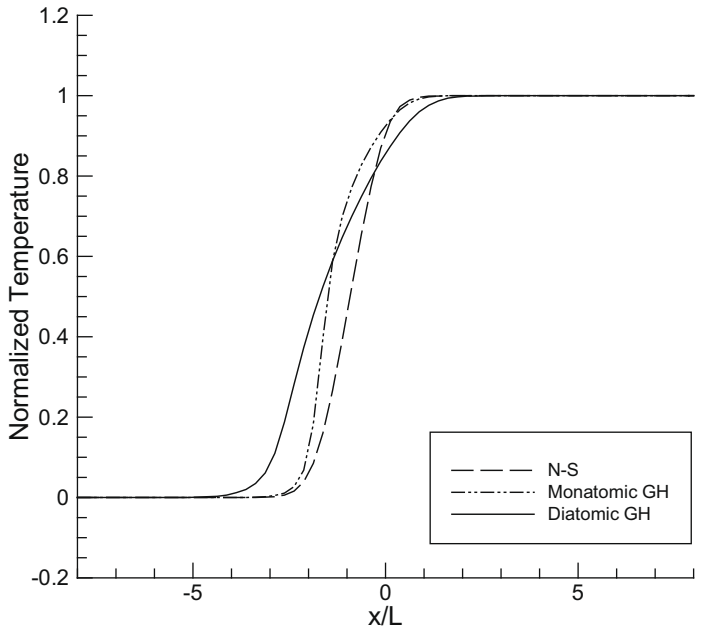

Fig. 4. Normalized temperature distribution for a diatomic gas($M = 6.1$).

where n_{N_2} and n_{O_2} represents the mole fraction of nitrogen and oxygen, respectively. Other species with very small number densities are ignored. The parameter β depends on the wall temperature T_w and the interfacial interaction parameter. For the case of the gas–surface interaction, β can be expressed as

$$\beta = \frac{Al}{k_B T} \exp\left(\frac{D_e}{k_B T_w}\right), \tag{63}$$

where A, D_e and l is the mean area of a site, the potential parameter and the mean free path, respectively. In many cases, the potential parameter D_e can be experimentally obtained. $D_e = 1.32$ kcal/mol is used for Ar–Al or N_2–Al molecular interaction

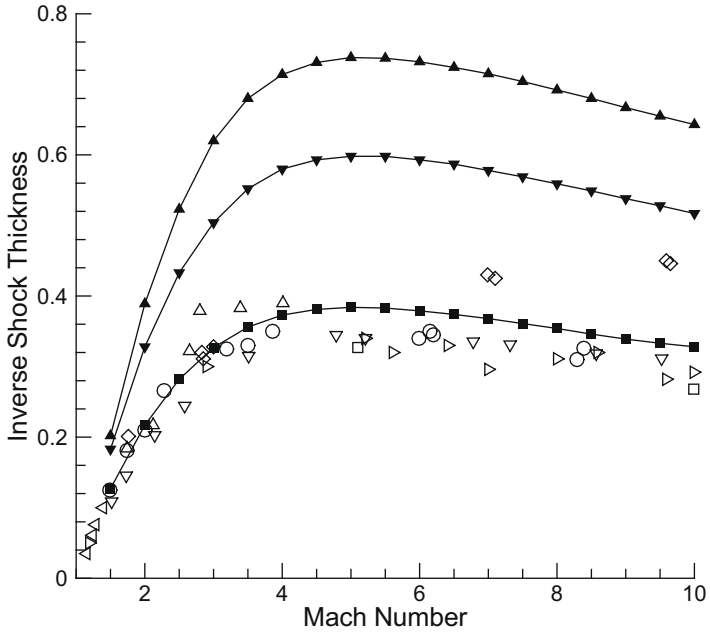

Fig. 5. Inverse shock density thickness for a diatomic gas (nitrogen, $s = 0.78$). Symbols are: (◁) by Greene and Hornig [30]; (△) by Linzer and Hornig [31]; (▷) by Camac [32]; (◇) by Robben and Talbot [33]; (○) by Alsmyer [34]. (□) represents the DSMC result by Boyd [35]. (▽) is the GH result by Al-Ghoul et al. [37]. Symbol (▲), (▼), (■) represents N–S, monatomic GH and diatomic GH, respectively.

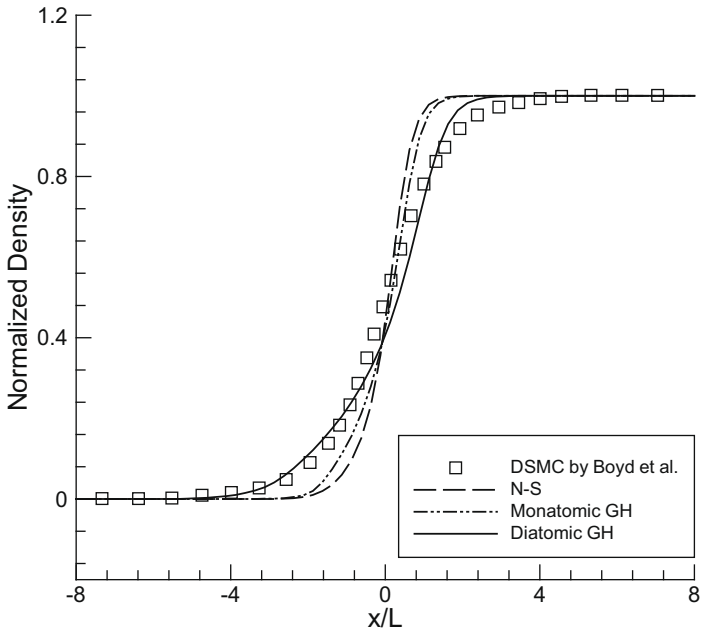

Fig. 6. Normalized density comparison with DSMC data ($M = 5.0$).

model. D_e for oxygen varies in the range of 3–8 kcal/mol according to the surface material and $D_e = 5$ kcal/mol is taken in the present work. The merit of the Langmuir boundary condition is that every parameter is determined without any tunable parameter.

The Maxwell–Smoluchowski boundary condition can be expressed as [25,26]

$$u_g - u_w = \frac{2-\sigma_v}{\sigma_v}\frac{1}{\rho(2RT_w/\pi)^{1/2}}\tau_s + \frac{3}{4}\frac{Pr(\gamma-1)}{\gamma\rho RT_w}(-Q_s), \tag{64}$$

$$T_g - T_w = \frac{2-\sigma_T}{\sigma_T}\frac{2(\gamma-1)}{\gamma+1}\frac{1}{\rho R(2RT_w/\pi)1/2}(-Q_n). \tag{65}$$

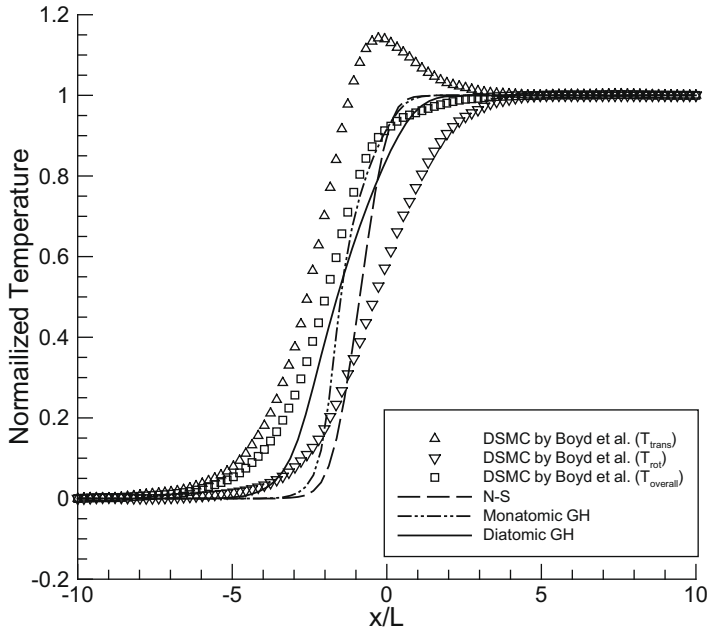

Fig. 7. Normalized temperature comparison with DSMC data ($M = 5.0$. As a reference, $T_{overall}$ is approximately obtained by $T_{overall} = (3T_{trans} + 2T_{rot})/5$).

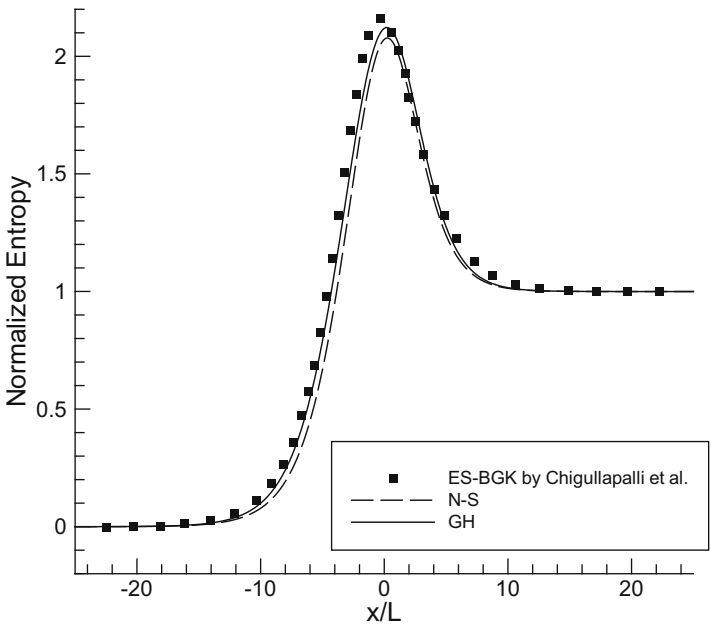

Fig. 8. Normalized entropy distribution for argon gas ($M = 1.4$). ES–BGK data are taken from the work by Chigullapalli et al. [39].

Q_s and Q_n are the tangential and normal heat transfer components in gas, and τ_s is the viscous stress component corresponding to the skin friction. R is the specific gas constant. σ_v and σ_T are the accommodation coefficients usually taking a value from 0.2 to 0.8. The term proportional to $(-Q_s)$ in Eq. (64) is associated with the thermal creep phenomenon, and it is ignored for constant wall temperature.

Furthermore, the second-order Maxwell boundary condition and the second-order boundary condition by Karniadakis and Beskok are employed [25,26]. The second-order Maxwell boundary condition can be expressed as

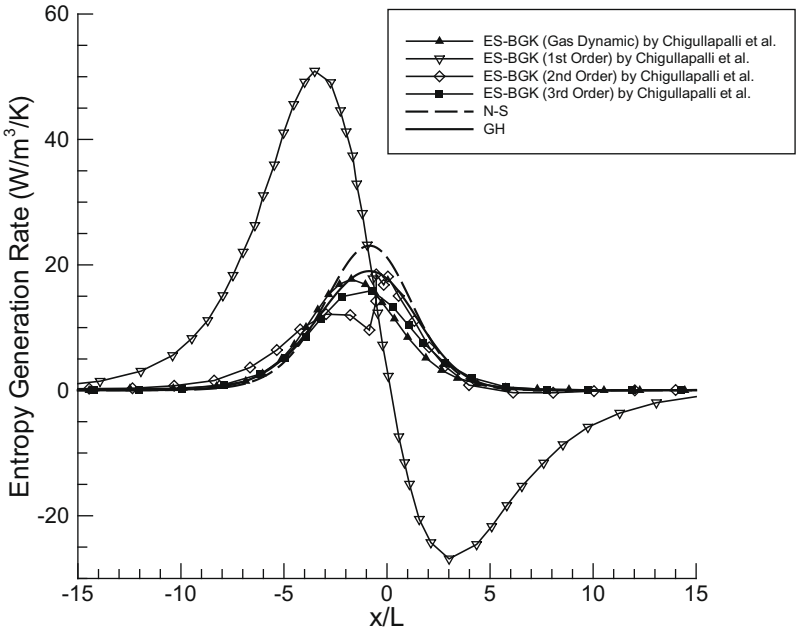

Fig. 9. Entropy generation rate distribution for argon gas ($M = 1.4$). ES–BGK data and gas dynamic data are taken from the work by Chigullapalli et al. [39].

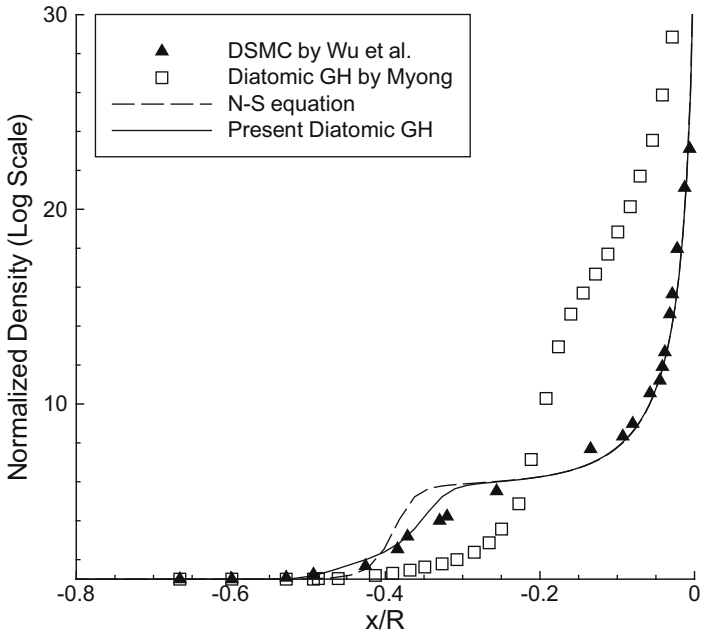

Fig. 10. Density profiles along the stagnation streamline ($x = 0$: stagnation point); the dashed and solid line is the N–S and diatomic GH result, respectively. Symbol represents the DSMC data (▲) by Wu et al. [38] and diatomic GH data (□) by Myong [7].

$$u_g - u_w = \frac{2-\sigma_v}{\sigma_v}\left[\frac{\mu}{\rho(2RT_w/\pi)^{1/2}}\frac{\partial u}{\partial n} + \frac{1}{2}\frac{\mu^2}{\rho^2(2RT_w/\pi)}\frac{\partial^2 u}{\partial n^2}\right], \tag{66}$$

$$T_s - T_w = \frac{2-\sigma_T}{\sigma_T}\frac{2(\gamma-1)}{\gamma+1}\left[\frac{k}{\rho R(2RT_w/\pi)^{1/2}}\frac{\partial T}{\partial n} + \frac{k\mu}{2\rho^2 R(2RT_w/\pi)}\frac{\partial^2 T}{\partial n^2}\right]. \tag{67}$$

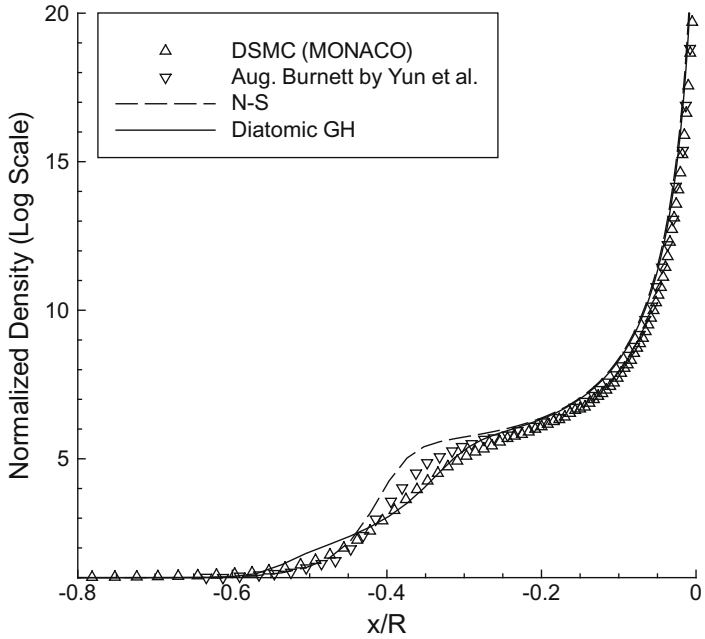

Fig. 11. Density profiles along the stagnation streamline ($x = 0$: stagnation point).

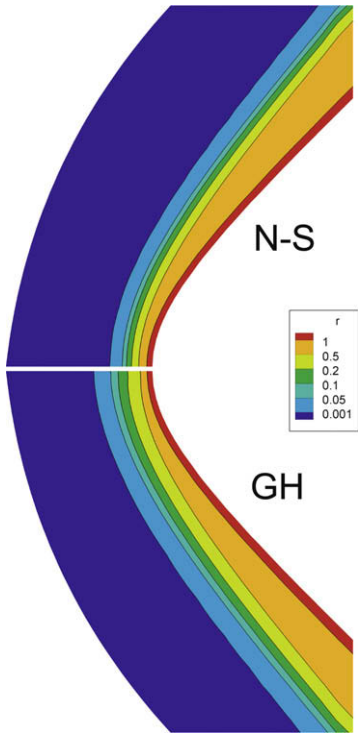

Fig. 12. Nondimensionalized density contours (log-scaled) by multi-species N–S and multi-species GH solvers.

The second-order boundary condition by Karniadakis and Beskok can be represented as

$$u_g - u_w = \frac{2-\sigma_v}{\sigma_v}\left[\frac{\mu}{\rho(2RT_w/\pi)^{1/2}}\frac{\partial u}{\partial n} + \frac{\mu^2\frac{\partial u}{\partial n}}{2\rho^2(2RT_w/\pi)\frac{\partial u}{\partial n} - \mu\rho(2RT_w/\pi)^{1/2}\frac{\partial^2 u}{\partial n^2}}\frac{\partial^2 u}{\partial n^2}\right]. \tag{68}$$

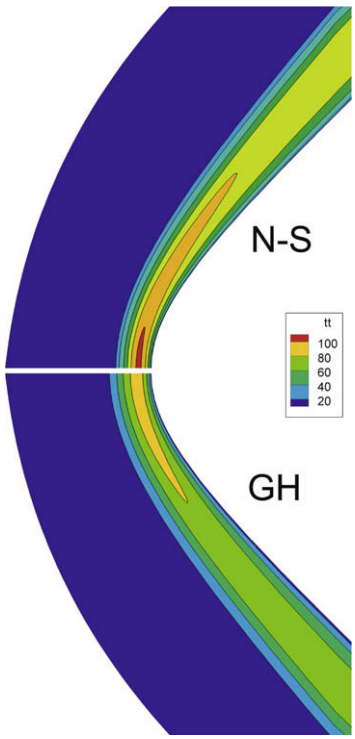

Fig. 13. Nondimensionalized temperature contours by multi-species N–S and multi-species GH solvers.

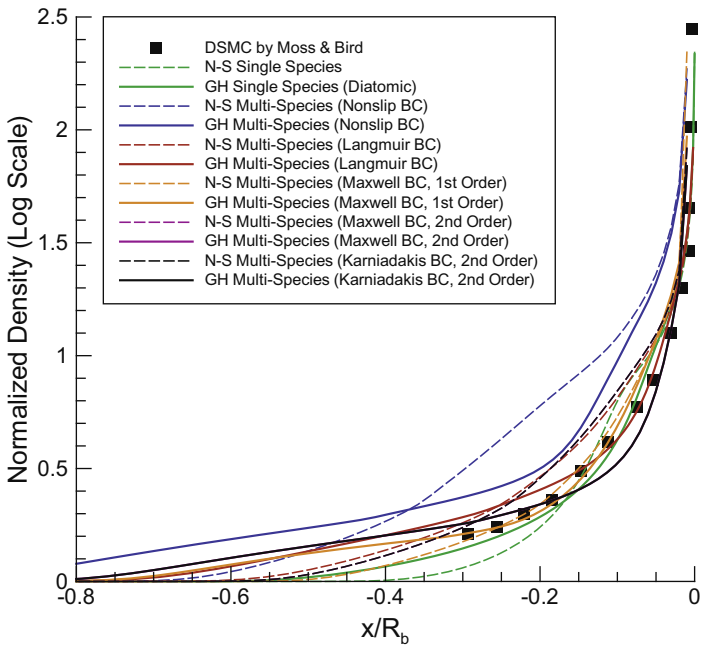

Fig. 14. Density distributions along the stagnation streamline ($x = 0$: stagnation point).

The temperature boundary condition is the same as Eq. (67). The effects of the boundary conditions will be discussed in Section 4.2.

4. Numerical methods and computational results

The multi-species N–S solver including chemical reaction model is used as a baseline solver. The multi-species GH solver is obtained by adding the multi-species GH constitutive relations combined with the Broydn nonlinear iterative solver [27]

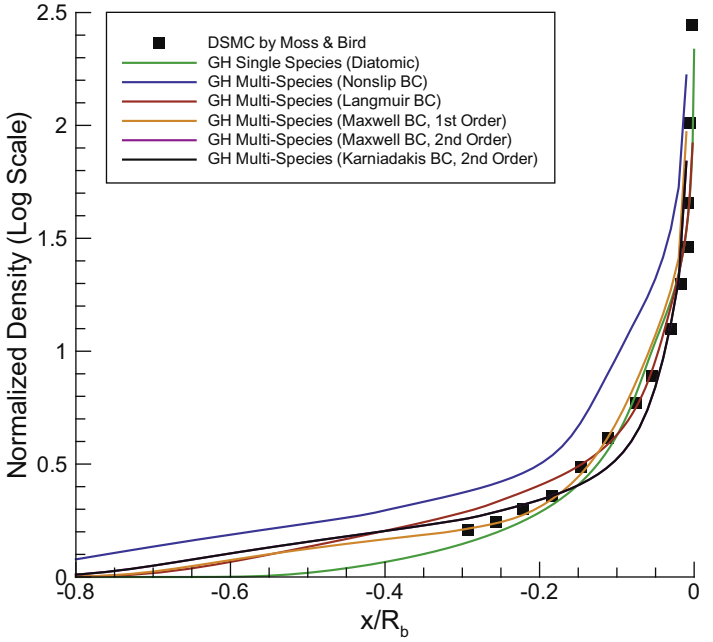

Fig. 15. Density distributions (GH results only) along the stagnation streamline ($x = 0$: stagnation point).

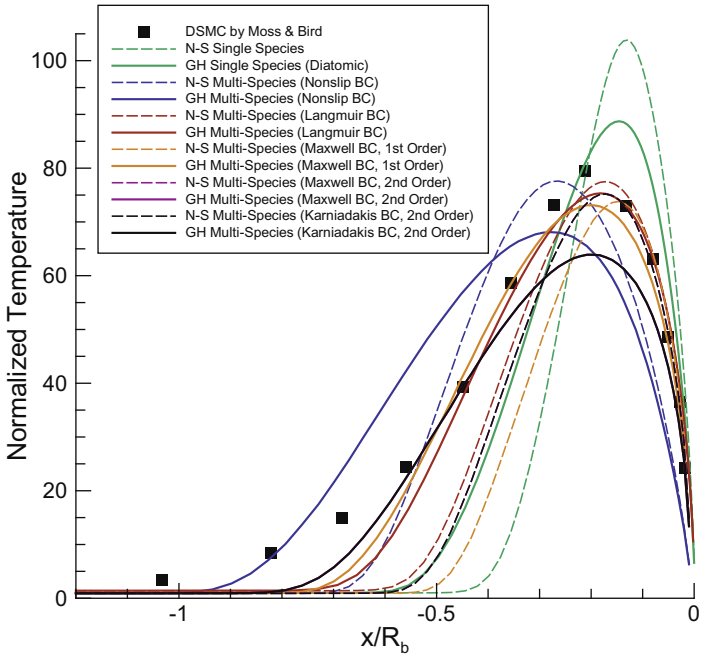

Fig. 16. Temperature distributions along the stagnation streamline ($x = 0$: stagnation point).

into the multi-species N–S solver. The computational code employs accurate and efficient numerical techniques based on finite volume method. As a cell-interface numerical flux, AUSMPW+, which is an improved AUSM-type scheme, is used [28]. The second-order MUSCL with van Albada limiter is used to avoid numerical oscillation, and the LU-SGS scheme is adopted as a time integration method. Since chemical and rarefied nonequilibrium effects cause small time step and slow convergence, a four-level multi-grid method with parallel computing is used to minimize computational load. Chemical source term is implicitly treated with the diagonal term of the source term Jacobian matrix $(\partial \mathbf{S}/\partial \mathbf{Q})$.

The multi-species GH solver has been developed by the step-by-step strategy. Starting from the one-dimensional diatomic single species GH solver, it has been expanded into the two-dimensional and axisymmetric single species GH solver

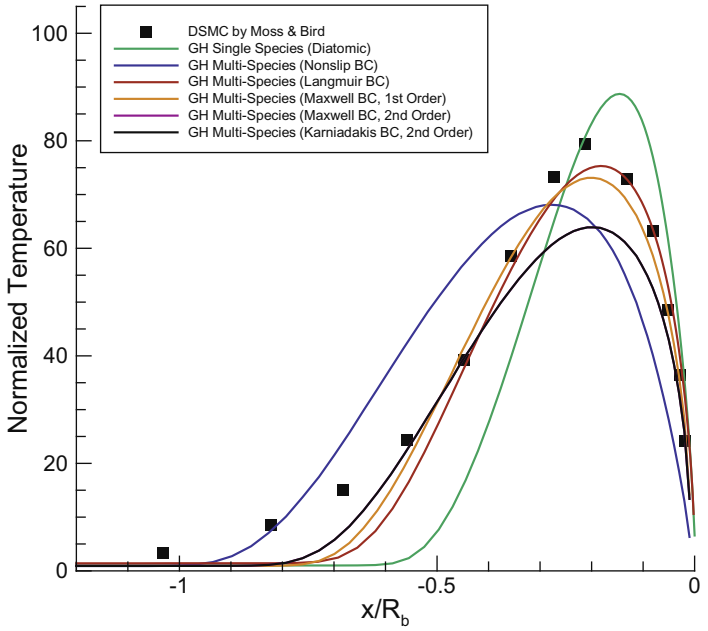

Fig. 17. Temperature distributions (GH results only) along the stagnation streamline ($x = 0$: stagnation point).

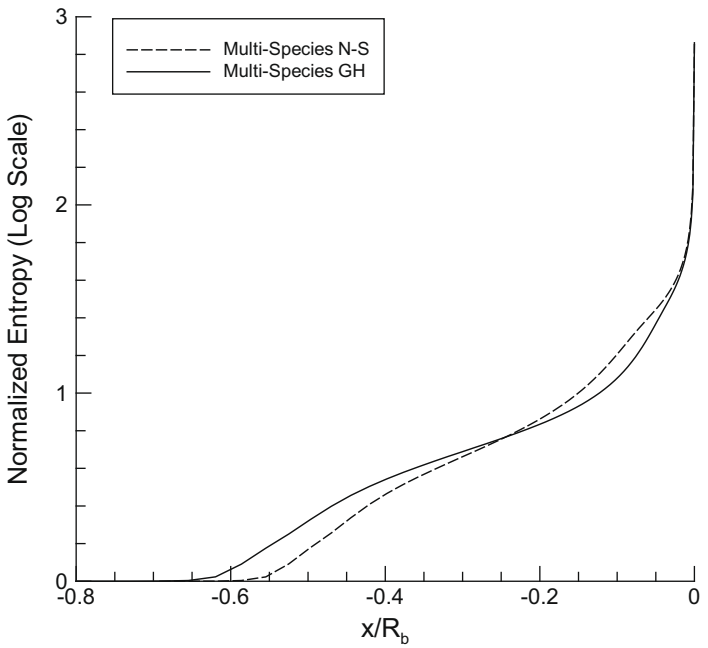

Fig. 18. Normalized entropy distribution (S/S_∞) along the stagnation streamline ($x = 0$: stagnation point).

for diatomic gas, and the axisymmetric multi-species GH solver. Each GH solver has been critically examined through suitable validation test cases.

4.1. Validation of the GH solvers for single species gases

Since the accuracy of the multi-species GH solver depends on that of single species monatomic and diatomic GH solvers, the performance of the diatomic GH solver is firstly examined. One-dimensional normal shock wave structure is computed using the one-dimensional diatomic GH solver. The Knudsen number is fixed as 1, and the Reynold number is calculated by Eq. (69) for the inflow Mach number of 1–10 [29]:

$$Kn = \sqrt{\frac{\gamma\pi}{2}}\frac{M}{Re}. \tag{69}$$

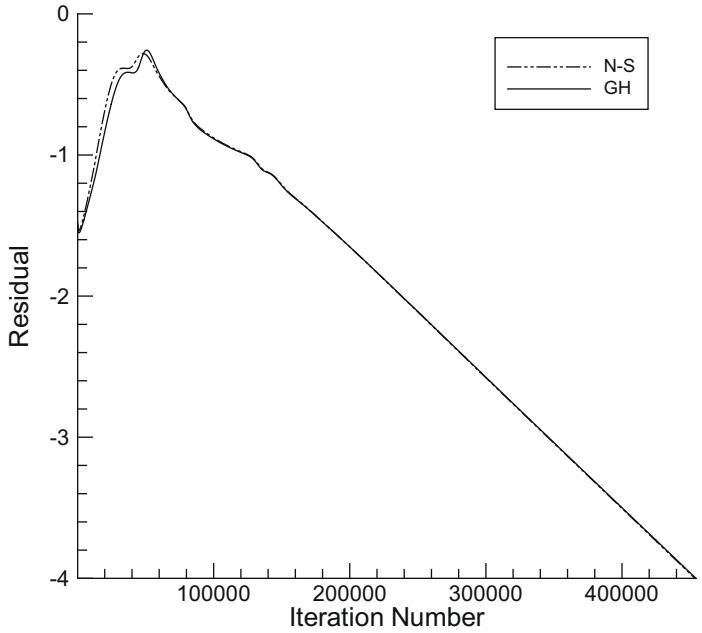

Fig. 19. Error history curves of the N–S and GH equations. CFL number is 0.01.

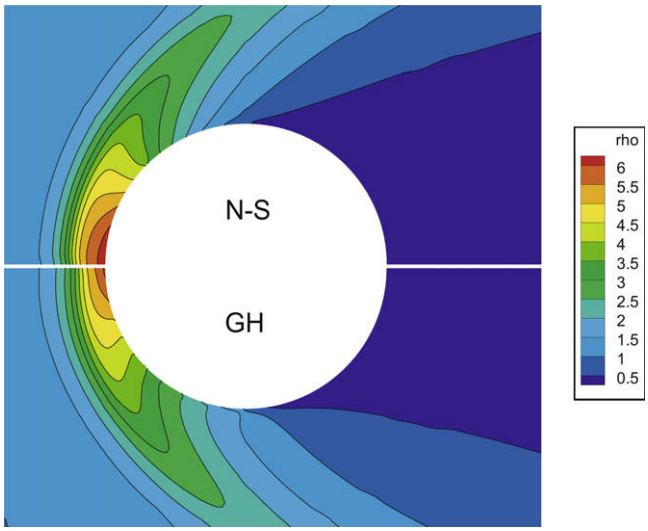

Fig. 20. Normalized density contours around the sphere.

For nitrogen gas, the viscous power law ($\mu = T^{v}$) is used with the exponent of $v = 0.78$. The computed results of the normalized density and temperature distributions for $M = 2.0$ and 6.1 are presented in Figs. 1–4. In Figs. 1 and 3, the diatomic GH result is the closest to the experimental data, compared with the N–S and monatomic GH results. As seen in Figs. 1 and 2, the present diatomic GH results agree well with the results by Al-Ghoul et al. [37].

The inverse shock thickness, which is one of the important parameters characterizing the shock wave structure, is depicted in Fig. 5. The inverse shock thickness is defined as follows:

$$\frac{1}{\delta} = \frac{|d\rho/dx|_{max}}{\rho_2 - \rho_1}. \tag{70}$$

Compared with the N–S and monatomic GH results, the diatomic GH equations provide the closest result to many experimental data [30–34] as well as the DSMC result [35]. In addition, the present GH result agrees well with the computation by Al-Ghoul et al. [36,37]. The normalized density and overall temperature distributions are also compared with the DSMC results. As shown in Figs. 6 and 7, the multi-species GH results show a good agreement with the DSMC data [35].

To examine the entropy characteristic, the normalized entropy and entropy generation rate of the one-dimensional normal shock are compared with the work by Chigullapalli et al. [39]. The test gas is argon. The entropy is calculated by [40]

$$S - S_0 = \rho R\left[\frac{1}{\gamma - 1}\ln\left(\frac{T}{T_0}\right) - \ln\left(\frac{\rho}{\rho_0}\right)\right], \tag{71}$$

and the entropy generation rate is calculated by [39,40]

$$\dot{S} = \frac{\Phi_{vis}}{T} + \frac{\mu}{Pr}\frac{\gamma R}{\gamma - 1}(\nabla T \cdot \nabla T), \tag{72}$$

where Φ_{vis} is the viscous dissipation function.

Figs. 8 and 9 show the normalized entropy distribution and the entropy generation rate. In Fig. 8, there is no significant difference among the ES–BGK, GH and N–S results, but the GH result shows a slightly faster rise of entropy than the N–S result. In Fig. 9, the GH result shows quite a reasonable rate compared with the third order ES–BGK result.

From the comparisons of one-dimensional tests, we can observe that the GH results are much more accurate than the N–S results and agree well with experimental or DSMC data.

The two-dimensional GH solver for diatomic single species gas is applied to the hypersonic rarefied flow over a cylinderical geometry. Two different inflow conditions are tested. The first is the same as in Ref. [7]: $M_\infty = 20$, $Kn_\infty = 0.05$, $Re_\infty = 593$, $T_w = 291.6$ K and $T_\infty = 20$ K. The length scale is normalized by the cylinder radius. In Fig. 10, the log-scaled density distribution along the stagnation streamline is depicted. The present diatomic GH result yields a very closer result to the DSMC result by Wu et al. [38] than other computations.

The second case is the same as in Ref. [41]: $M_\infty = 10$, $Kn_\infty = 0.1$, $Re_\infty = 148.3$, $T_w = 208.4$ K and $T_\infty = 1000$ K. The DSMC result is obtained by the authors using the MONACO Ver. 2.0 with the variable hard sphere (VHS) molecular model. The accommodation coefficient for wall boundary condition is set to be 1 (fully accommodated) as in Ref. [41] for comparison purpose. Since the DSMC boundary condition has a different mechanism from the Langmuir boundary condition (MONACO

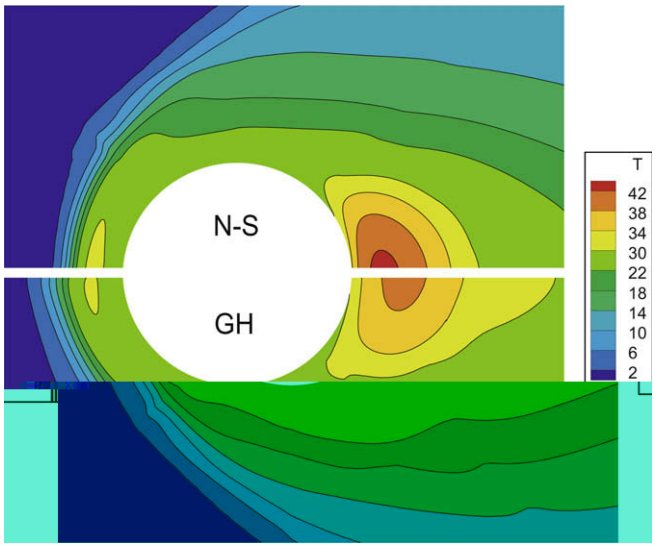

Fig. 21. Normalized temperature contours around the sphere.

has the accommodation coefficient while the Langmuir boundary condition does not), we cannot guarantee that the two boundary conditions are fully compatible. Even in this case, the diatomic GH result with the Langmuir boundary condition shows a better agreement with the DSMC data than the Burnett equation result with the Maxwell boundary condition of the accommodation coefficient 1 [41]. However, more investigation on the parameters of the Langmuir boundary condition which are consistent with the GH theory is necessary.

The log-scaled density profile along the symmetric axis is shown in Fig. 11. Compared with the Augmented Burnett and N–S data, the diatomic GH result yields a relatively larger shock thickness, and it is the closest to the DSMC data. The larger shock thickness is a typical phenomenon in nonequilibrium rarefied flows. Low density causes the mean free path of gas molecules to increase, and the molecules experience less collision. As a result, it takes a longer time to reach the equilibrium state, and the molecules travel a distance as long as the shock thickness.

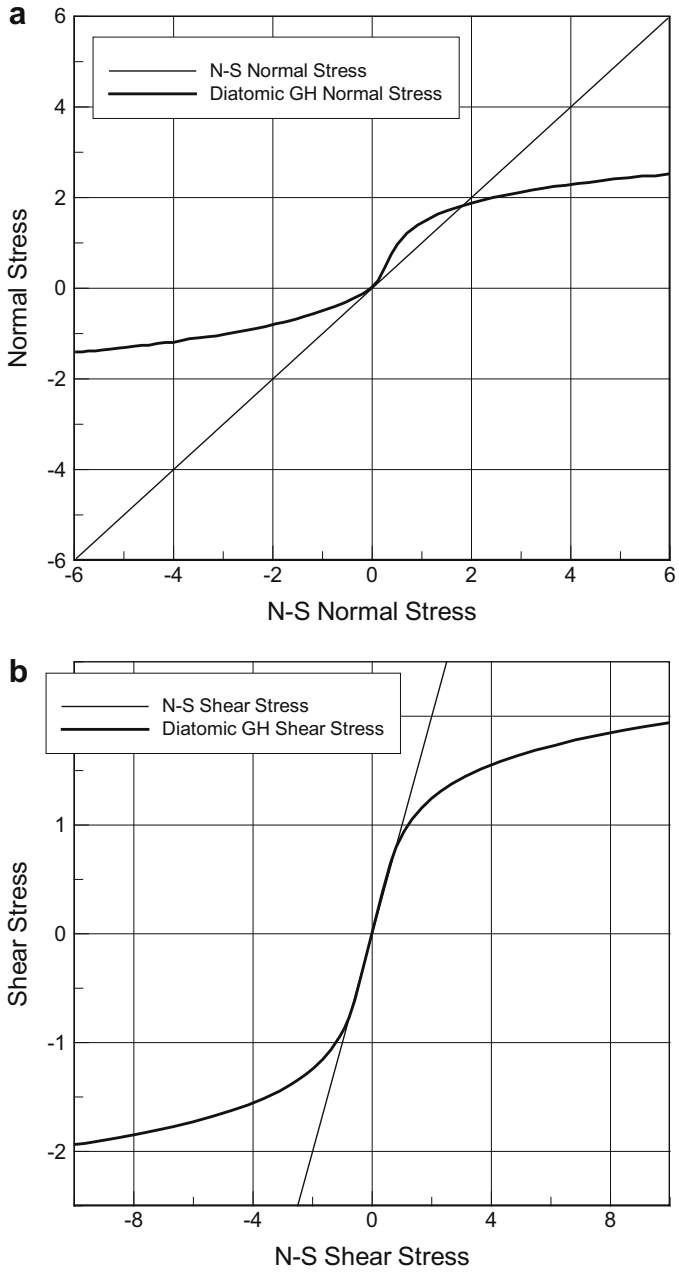

Fig. 22. Comparison of the N–S and GH stress distributions: (a) normal stress; (b) shear stress [7].

From the comparisons, it can be seen that the present diatomic GH computational model properly describes the nonequilibrium flow physics.

4.2. Multi-species test case 1: a space shuttle nose flow

The multi-species GH computational model is applied to hypersonic rarefied flows over a space shuttle nose, a sphere, and a reentry body. The first test case is a space shuttle nose. The geometry is axisymmetric, and the cross section along the axis is hyperbola, which has a nose radius of 1.362 m and an asymptotic half angle of 42.5°. The grid system is 51×81, and it is normalized by the nose radius. The inflow condition, geometry and DSMC data are taken from the work by Moss and Bird [42]. The inflow condition is $M_\infty = 25.3,\ Kn_\infty = 0.227,\ Re_\infty = 170,\ T_w = 223$ K and $T_\infty = 560$ K.

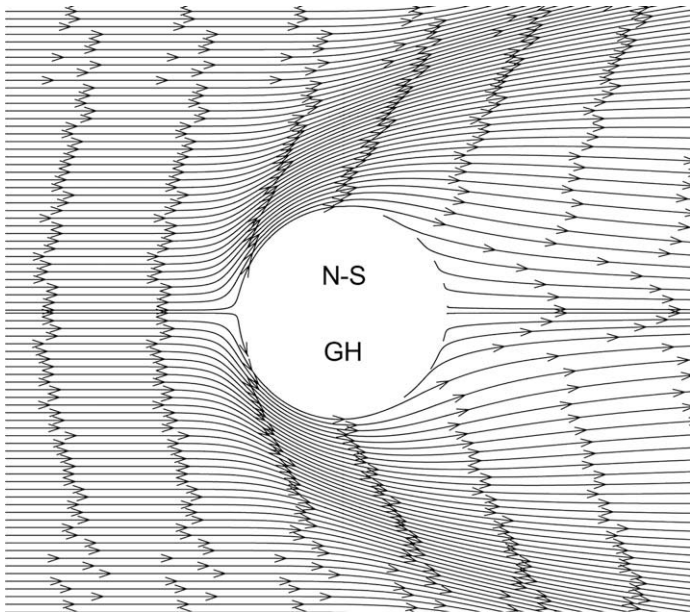

Fig. 23. Streamline pattern around the sphere.

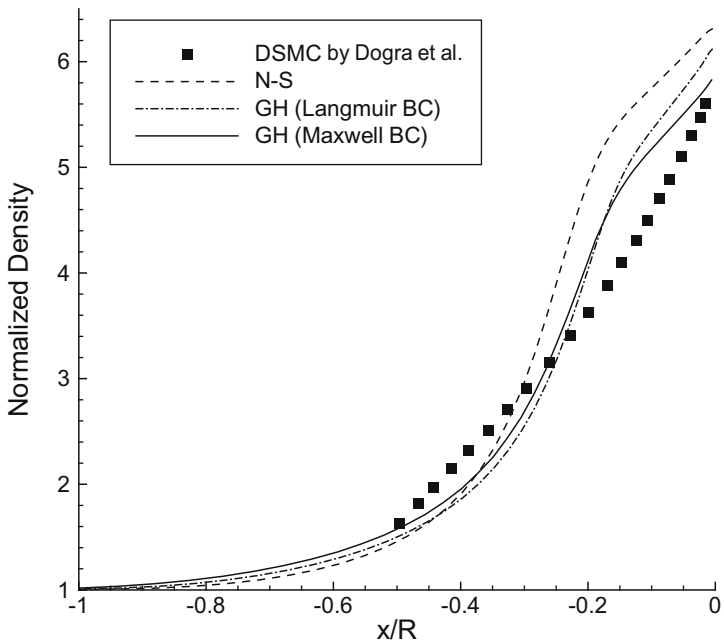

Fig. 24. Density distributions along the stagnation streamline.

Four solvers were tested: the N–S solvers for single and multi-species gas, the diatomic GH solvers for single and multi-species gas. Fig. 12 shows the log-scaled density contours obtained by the multi-species N–S and GH solvers. Two results are quite different in terms of shock front position and shock thickness. The shock thickness along the symmetric axis is thicker in the GH model. In Fig. 13, temperature contours are compared, which are also different owing to the nonequilibrium effect. The log-scaled density and temperature distributions along the stagnation streamline are compared in Figs. 14–17, and the GH results are particularly depicted in Figs. 15 and 17 for clarity. It is seen that the GH results are closer to DSMC for every boundary condition. This strongly supports the superior validity of the GH equations.

Both the Maxwell condition and the Langmuir condition provide the results comparable to DSMC data, although the internal structures of the two conditions are somewhat different. While the Maxwell boundary condition includes the density-

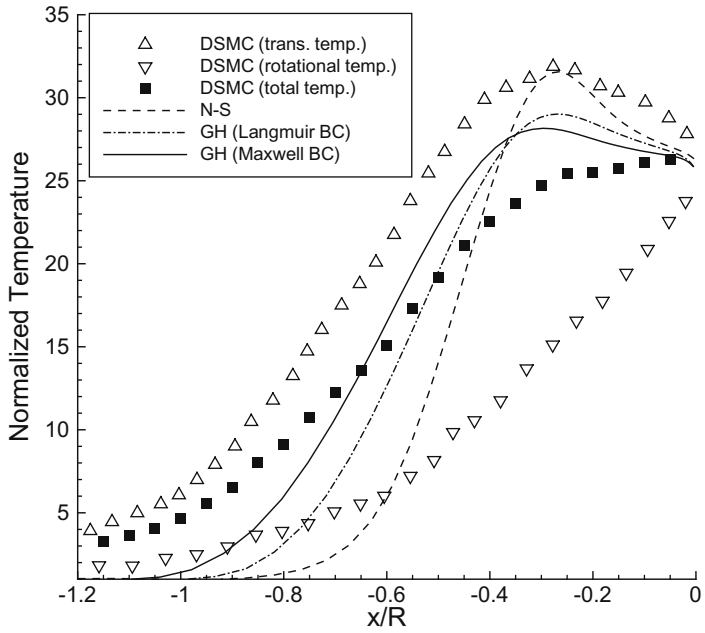

Fig. 25. Temperature distributions along the stagnation streamline. DSMC data are taken from Ref. [43] by Dogra et al.

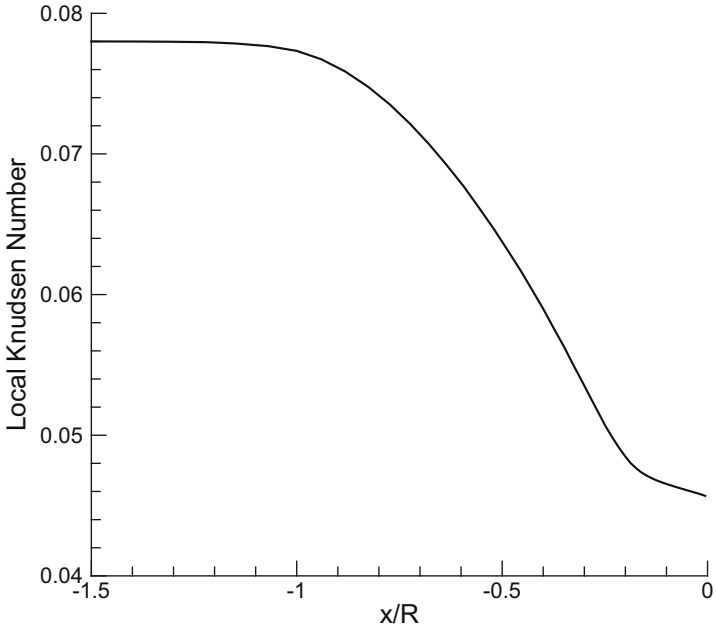

Fig. 26. Local Knudsen number distribution along the stagnation streamline.

dependent term and the gradient of velocity and temperature, the Langmuir boundary condition does not contain these terms. Considering that the Langmuir boundary condition does not require any tunable parameter, the accuracy and/or robustness of the GH solver is expected to be further improved by exploring a more accurate formulation (especially, the temperature condition) and the exact potential parameter value (D_e).

In Figs. 16 and 17, the second-order Maxwell boundary condition produces a lower peak value, a faster arising and more diffused temperature distribution than the first-order Maxwell boundary condition. The reason is that the coefficients of the second terms in Eqs. (66) and (67) correspond to the square of Knudsen number, which induce a larger velocity-slip and temperature-jump as Knudsen number increases. The second-order boundary condition by Karniadakis and Beskok is as good as the second-order Maxwell boundary condition. It appears that the influence of higher-order terms is dominant in the temperature condition (Eq. (67)) rather than the velocity conditions (Eqs. (64) and (66)).

From the log-scaled density profile in Figs. 14 and 15, the DSMC data indicate most of mass flow is concentrated near the front surface. Under this nonequilibrium condition, molecules cannot experience sufficient collisions until they reach the nose surface. Slopes of the density curves indicate that the N–S model predicts superfluous molecular collisions, which suggests that the multi-species GH results are more consistent with the nonequilibrium physics of rarefied flows.

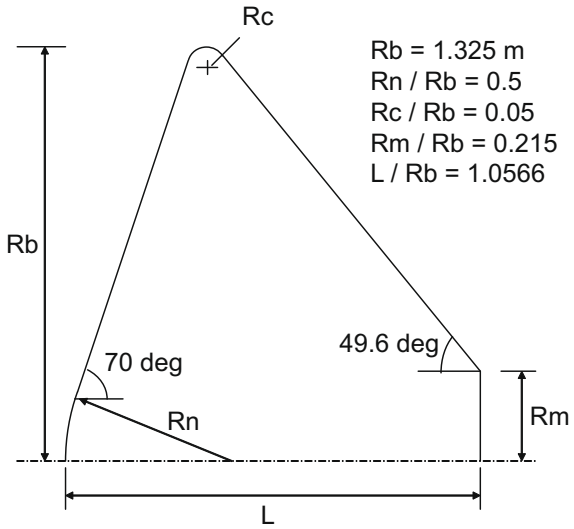

Fig. 27. Geometry of a reentry body [44].

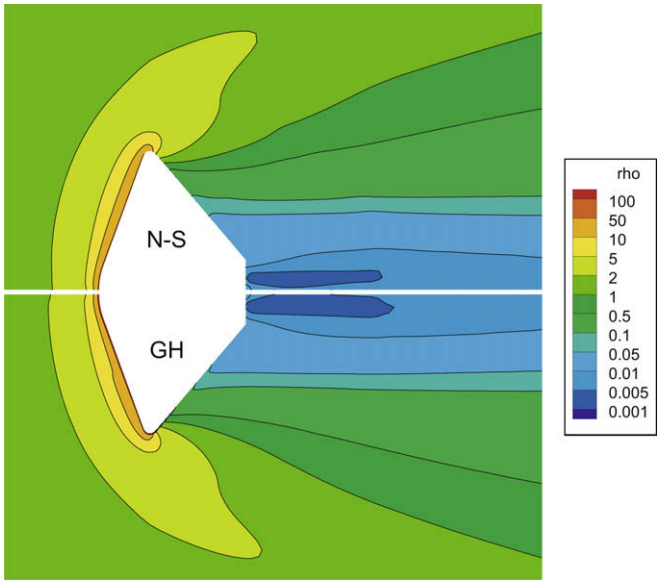

Fig. 28. Normalized density contours around the reentry body.

By using Eq. (2), the normalized entropy distribution along the stagnation streamline is compared in Fig. 18. The GH entropy varies earlier than the N–S entropy, which is consistent with density and temperature distributions. Also, the overall slope of the GH entropy is lower than that of the N–S entropy.

In addition, computational efficiency and convergence characteristic of the multi-species GH equations are examined. Fig. 19 shows the residual history of the multi-species GH and N–S equations with CFL = 0.01. The total number of iteration is almost the same but the GH solver requires about three times more computational cost. This is caused by the Broydn nonlinear solver, which computes the heavily coupled GH constitutive relations by an iterative algorithm. The computing time of the GH solver can be significantly reduced if N–S results are used as initial conditions and a faster nonlinear equation solver is employed. Compared to other computational approaches, such as DSMC, Burnett equations or Grad's moment method, computational cost of the GH solver is still quite efficient.

4.3. Multi-species test case 2: hypersonic rarefied flow over a sphere

The inflow condition is $M_\infty = 11.25,\ Kn_\infty = 0.078,\ Re_\infty = 15.16,\ T_w = 600$ K and $T_\infty = 22.8$ K, which is taken from the DSMC computation by Dogra et al. [43]. The grid system is 97×161. The four-level multigrid and parallel computation

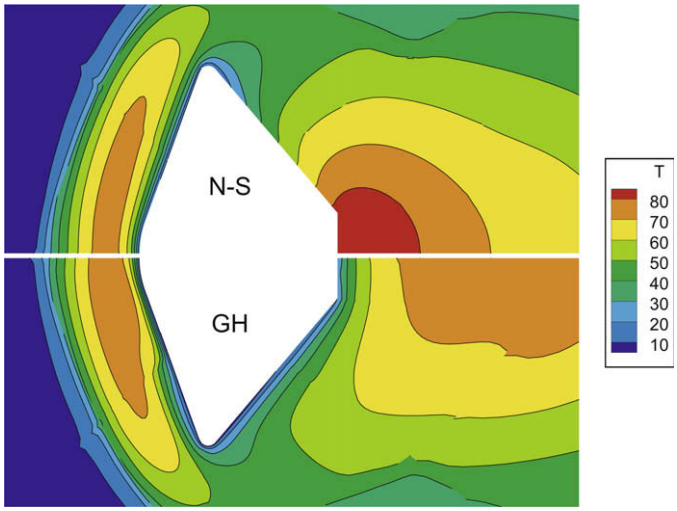

Fig. 29. Normalized temperature contours around the reentry body.

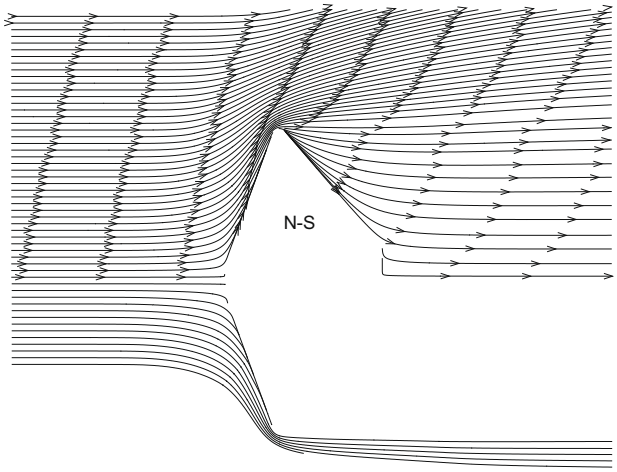

are utilized for convergence acceleration. Figs. 20 and 21 show the density and temperature contour, respectively. In Fig. 20, the multi-species GH result is highly rarefied at the wake region, and at the same time it is more diffused, which is physically reasonable compared to the DSMC result [43]. In Fig. 21, the GH result shows a larger shock thickness in front of the stagnation point and a lower temperature distribution at the wake region. This is because, as shown in Fig. 22, the magnitude of the GH stress is asymptotically finite, which has been observed earlier in Refs. [7,15]. The asymptotic behavior of the GH stress triggers an earlier rise of non-continuum flow characteristics, while the N–S stress seems to be too large to predict non-continuum flow characteristics. Considering that the stress under rarefied flow condition is usually limited to a finite value due to less frequent molecular collisions, the asymptotic stress behavior of the GH model is one of the factors to produce the closer results to the DSMC data. In Fig. 23, streamline pattern shows that no vortex is formed at the wake region, which is caused by very low molecular population. The local mean free path increases so that molecules can expand without much collision.

The normalized density and temperature distributions along the stagnation streamline are plotted in Figs. 24 and 25. The local Knudsen number is also depicted in Fig. 26, which is calculated by

$$Kn_{local} = \sqrt{\frac{\gamma\pi}{2}}\frac{M_{local}}{Re_{local}}.$$

In Fig. 25, the overall temperature of the DSMC result, obtained from the following approximate relation in Ref. [6], is presented.

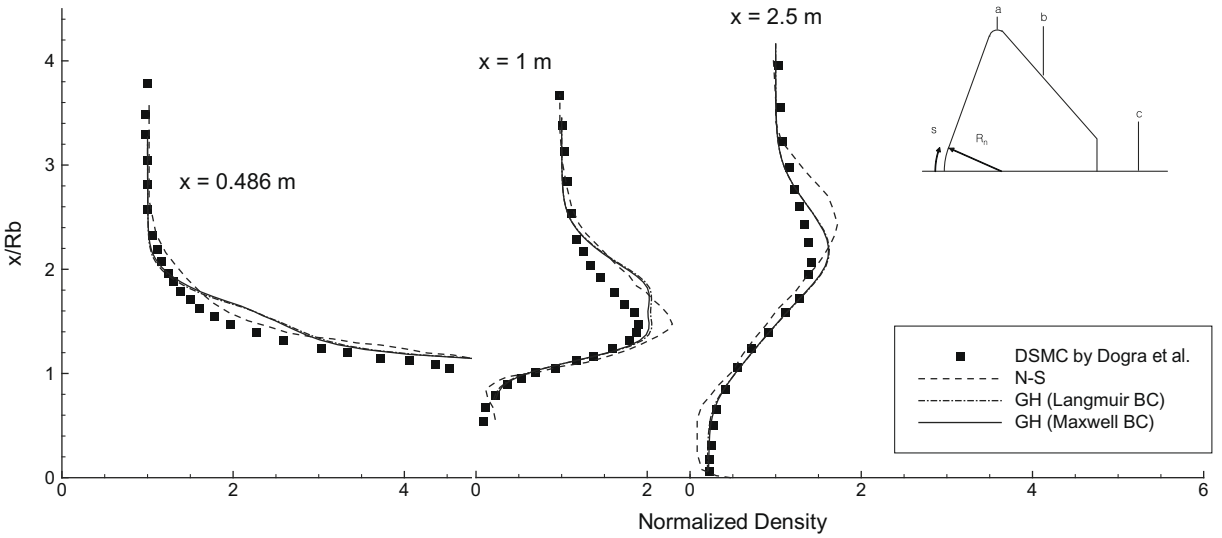

Fig. 31. Density distributions in the wake region of the reentry body.

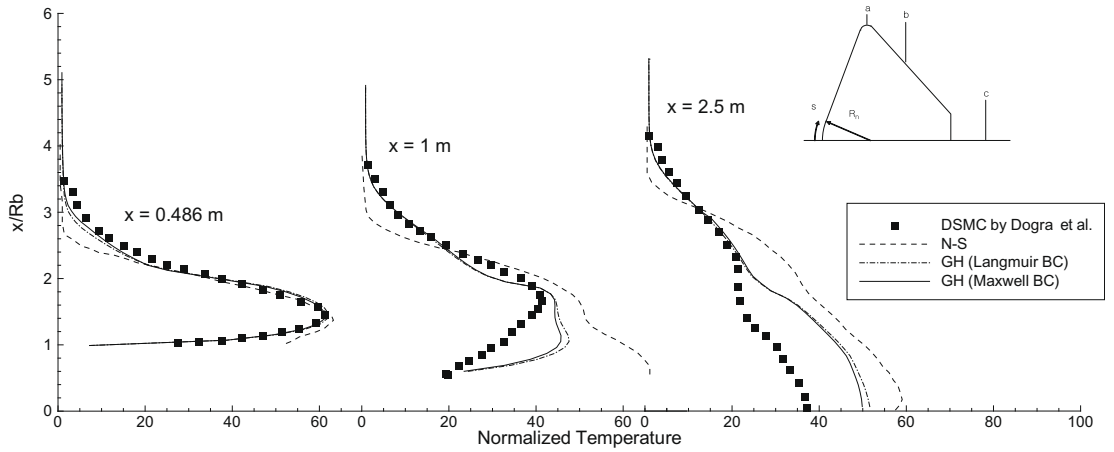

Fig. 32. Temperature distributions in the wake region of the reentry body.

$$T_{average} = \frac{3T_{trans} + \zeta T_{int}}{3 + \zeta}.$$

ζ is the number of degrees of freedom of internal energy, which is two in this test case since rotational energy plays a dominant role. Although the accuracy of the overall temperature is not fully guaranteed, it can be used as a reference value to check the qualitative trend. Overall temperature distribution of the multi-species GH result with the Maxwell–Smoluchowski boundary condition shows a fairly good agreement with the DSMC data. However, some deviations can be observed in terms of the peak value and the curve slope. As mentioned in the derivation of the GH computational model in Section 2.1, this is related to the approximation of the collision bracket integrals ($\Re_{ij}^{(\alpha\beta)}$ or $R_{ij}^{(\alpha\beta)}$) and the slip-wall boundary conditions. As shown in Eqs. (20)–(23), the collision bracket integrals are calculated not completely but approximately for the purpose of computation efficiency. A more elaborate approximation of the collision bracket integrals is essential to enhance computational accuracy. The other aspect is to improve the accuracy of the slip-wall boundary conditions. As shown in Section 4.2, the choice of a slip-wall boundary condition brings a substantial difference. More investigation on slip boundary conditions fit to the multi-species GH equations is certainly necessary.

4.4. Multi-species test case 3: hypersonic rarefied flow over a reentry body

The final test case of the multi-species GH computational model is a reentry body problem. The focus of this test is to evaluate expansion characteristics of the GH model at the wake region under highly rarefied flow condition. Fig. 27 shows the geometry of the reentry body in Dogra's work [44]. The inflow condition is $M_\infty = 23.47$, $Kn_\infty = 0.2238$, $Re_\infty = 155.5$, $T_w = 1000$ K and $T_\infty = 211.1$ K, which represents the 105 km-altitude condition of air. Fig. 28 shows the density contour of the N–S and multi-species GH solvers. There seems to be no particular difference. In Fig. 29, however, the temperature predicted by the multi-species GH equations is much lower than that of the N–S equations, especially in the wake region. Fig. 30 shows a vortex-free streamline pattern around the reentry body.

To quantitatively examine the computational accuracy of the multi-species GH equations, the density and temperature distributions at the wake region are compared with the DSMC and N–S data in Figs. 31 and 32. Though some differences are observed, the GH results are closer to the DSMC data. In particular, the tendency of the temperature distribution by the N–S equations is grossly deviated from the DSMC data. Fig. 33 shows the pressure distribution along the reentry body surface. The pressure on the rear side of the reentry body drastically decreases by highly rarefied flow condition. Compared to the N–S result, the GH result with the Maxwell–Smoluchowski boundary condition yields a fairly good agreement with the DSMC data even at the wake region. However, some deviations are still observed. Fig. 34 shows the local Knudsen number distribution along the reentry body surface, which is abruptly increasing due to the rapid flow expansion behind the cor-

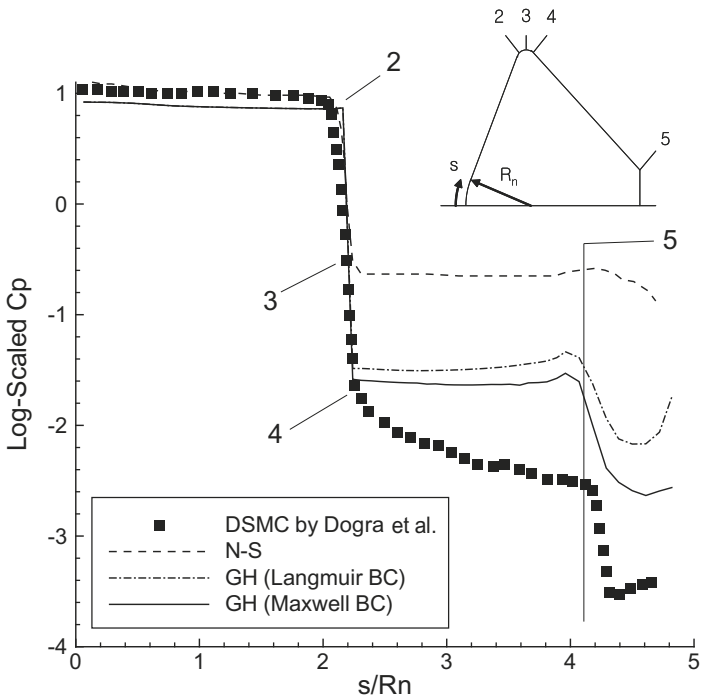

Fig. 33. Pressure coefficient distributions along the reentry body surface.

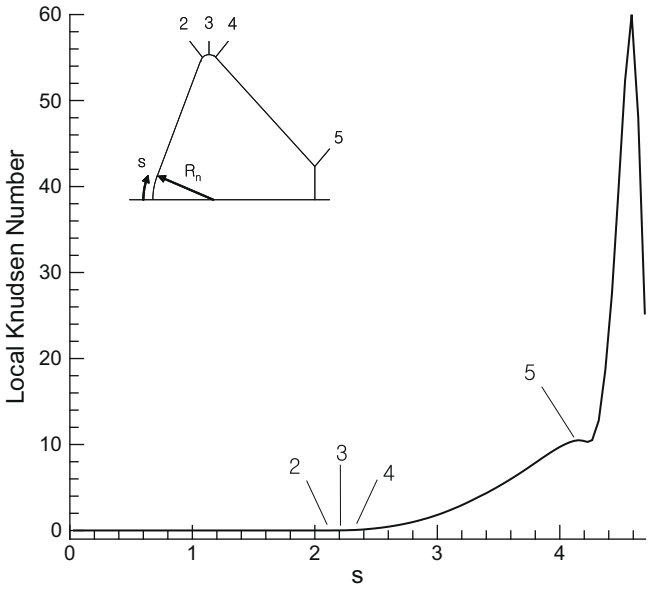

Fig. 34. Local Knudsen number distributions along the reentry body surface.

ner. The small Knudsen number approximation of the collision bracket integrals seems to be one of the limitations in dealing with locally high-rarefied flows.

5. Conclusion

For efficient computations of hypersonic rarefied gas flows, the multi-species generalized hydrodynamic computational model is developed. It is established by combining two GH equations: one is the monatomic multi-species GH theory and the other is the diatomic single species GH theory. The constitutive relations of the multi-species GH theory are consistent with the second law of thermodynamics. In derivation process, the dissipation term related to the positive entropy production is explicitly determined in terms of the nonconserved variables. The heterogeneous collision between monatomic and diatomic molecules is deliberated in the diffusion modeling. With the multi-species GH theory, the GH rarefied flow solver is extended into an axisymmetric formulation.

By simulating hypersonic flows over axisymmetric bodies, it is observed that the present multi-species GH solver is more robust and yields closer results to the DSMC data than other continuum-based solvers. By incorporating nonequilibrium effects such as chemical reaction and rarefaction effects, the multi-species GH computational model showed an enhanced accuracy than existing single species GH models.

At the same time, some deviations from the DSMC data are still observed, which indicates a room for more elaboration in dealing with highly nonequilibrium flows. It suggests that more sophisticated computation of the collision bracket integrals and further development of the slip-wall boundary condition will greatly enhance the accuracy of the present GH computational model. Although the multi-species GH theory (one of the 'fluid dynamic models') currently does not catch up with DSMC ('full kinetic model') in terms of computational accuracy, the GH theory has a merit as a robust continuum-based model to efficiently analyze rarefied flows. Considering the fact that various advanced CFD techniques can be readily applied to the GH equations, the GH numerical model is expected to be improved near future.

Acknowledgments

The authors appreciate financial supports by Korea National Space Laboratory Program (Grant S10801000121-08A0100-12110), and by the Brain Korea-21 Program for the Mechanical and Aerospace Engineering Research at Seoul National University, and by the Korea Agency of Defence Development (ADD). The authors also appreciate financial and administrative helps from Institute of Advanced Aerospace Study.

Appendix A. Chemical reaction model

Five species air model containing N_2, O_2, N, O and NO is used [3,19,20]. For the reaction rate constant, Blottner's model is adopted. All of the details to implement the Blottner's model can be found in Ref. [45]:

$$
\begin{aligned}
&O_2 + \mathfrak{M} \leftrightarrow O + O + \mathfrak{M},\\
&N_2 + \mathfrak{M} \leftrightarrow N + N + \mathfrak{M},\\
&NO + \mathfrak{M} \leftrightarrow N + O + \mathfrak{M},\\
&O + NO \leftrightarrow N + O_2,\\
&O + N_2 \leftrightarrow N + NO,
\end{aligned}
$$

where $\mathfrak{M}$ can be any of the five possible collision partners.

In Eq. (53), ρ_i means the partial density of the ith species, and S_i is the composition change source term due to chemical reactions. $D_{c,i}$ is the chemical diffusion coefficient computed by

$$D_{c,i} = \frac{\mathcal{M}_i}{\mathcal{M}} \frac{1-\mathcal{C}_i}{1-\chi_i} \frac{\mu}{\rho S_c},$$

where S_c represents the Schmidt number. $\mathcal{M}$ is the molecular mass, $\mathcal{C}_i$ is mass fraction of the ith species, and χ_i is given by $\mathcal{C}_{c,i}(\mathcal{M}_i/\mathcal{M})$. The total viscosity and conductivity are calculated using Wilke's semi-empirical mixing rule [46].

$$\mu = \sum_i \frac{\mu_i \chi_i}{\mathfrak{F}_i}, \quad k = \sum_i \frac{k_i \chi_i}{\mathfrak{F}_i},$$

where μ_i can be defined by Blottner's model [45]

$$\mu_i = 0.1 \exp\left[(A_i \ln T + B_i)\ln T + C_i\right],$$

and for k_i, Eucken's relation is used [19]:

$$k_i = \mu_i \left(\frac{5}{2} C_{v,trans,i} + C_{v,rot,i}\right).$$

$\mathfrak{F}_i$ is given by

$$\mathfrak{F}_i = \sum_j \chi_j \left[1 + \sqrt{\frac{\mu_i}{\mu_j}} \left(\frac{\mathfrak{M}_j}{\mathfrak{M}_i}\right)^{1/4}\right]^2 \left[\sqrt{8\left(1 + \frac{\mathfrak{M}_i}{\mathfrak{M}_j}\right)}\right]^{-1}.$$

Appendix B. Axisymmetric components of the multi-species GH constitutive relations

In the following equations, u and v denotes the z- and r-directional velocity, respectively.

1. $[\mathbf{J}_i d_t \mathbf{u}]^{(2)}$ components:

$$
\begin{aligned}
[\mathbf{J}_i d_t \mathbf{u}]^{(2)}_{zz} &= J_{z,i}\left(u\frac{\partial u}{\partial z} + v\frac{\partial u}{\partial r}\right) - \mathfrak{A},\\
[\mathbf{J}_i d_t \mathbf{u}]^{(2)}_{zr} &= \frac{1}{2}\left[J_{z,i}\left(u\frac{\partial v}{\partial z} + v\frac{\partial v}{\partial r}\right) + J_{r,i}\left(u\frac{\partial u}{\partial z} + v\frac{\partial u}{\partial r}\right)\right],\\
[\mathbf{J}_i d_t \mathbf{u}]^{(2)}_{rr} &= J_{r,i}\left(u\frac{\partial v}{\partial z} + v\frac{\partial v}{\partial r}\right) - \mathfrak{A}, \quad [\mathbf{J}_i d_t \mathbf{u}]^{(2)}_{\theta\theta} = -\mathfrak{A},
\end{aligned}
$$

where

$$\mathfrak{A} = \frac{1}{3}\left[J_{z,i}\left(u\frac{\partial u}{\partial z} + v\frac{\partial u}{\partial r}\right) + J_{r,i}\left(u\frac{\partial v}{\partial z} + v\frac{\partial v}{\partial r}\right)\right].$$

2. $[\mathbf{\Pi}_i \cdot \nabla u]^{(2)}$ components:

$$
\begin{aligned}
[\mathbf{\Pi}_i \cdot \nabla u]^{(2)}_{zz} &= \Pi_{zz,i}\frac{\partial u}{\partial z} + \Pi_{rz,i}\frac{\partial u}{\partial r} - \mathfrak{B},\\
[\mathbf{\Pi}_i \cdot \nabla u]^{(2)}_{rz} &= \frac{1}{2}\left[\Pi_{zz,i}\frac{\partial v}{\partial z} + \Pi_{rr,i}\frac{\partial u}{\partial r} + \Pi_{rz,i}\left(\frac{\partial u}{\partial z} + \frac{\partial v}{\partial r}\right)\right],\\
[\mathbf{\Pi}_i \cdot \nabla u]^{(2)}_{rr} &= \Pi_{rz,i}\frac{\partial v}{\partial z} + \Pi_{rr,i}\frac{\partial v}{\partial r} - \mathfrak{B}, \quad [\mathbf{\Pi}_i \cdot \nabla u]^{(2)}_{\theta\theta} = \Pi_{\theta\theta,i}\frac{v}{y} - \mathfrak{B},
\end{aligned}
$$

where

$$\mathfrak{B} = \frac{1}{3}\left[\Pi_{zz,i}\frac{\partial u}{\partial z} + \Pi_{rr,i}\frac{\partial v}{\partial r} + \Pi_{rz,i}\left(\frac{\partial v}{\partial z} + \frac{\partial u}{\partial r}\right) + \Pi_{\theta\theta,i}\frac{v}{r}\right].$$

3. $(\mathbf{\Pi}_i + \omega f_b \Delta_i \mathbf{I}) : \nabla u$ component:

$$(\mathbf{\Pi}_i + \omega f_b \Delta_i \mathbf{I}) : \nabla u = (\Pi_{zz,i} + \omega f_b \Delta_i)\frac{\partial u}{\partial z} + (\Pi_{rr,i} + \omega f_b \Delta_i)\frac{\partial v}{\partial r} + \Pi_{rz,i}\left(\frac{\partial v}{\partial z} + \frac{\partial u}{\partial r}\right).$$

4. $(d_t\mathbf{u}) \cdot \mathbf{J}$ component:

$$(d_t\mathbf{u}) \cdot \mathbf{J}_i = J_{z,i}\left(u\frac{\partial u}{\partial z} + v\frac{\partial u}{\partial r}\right) + J_{r,i}\left(u\frac{\partial v}{\partial z} + v\frac{\partial v}{\partial r}\right).$$

5. $\mathbf{J}_i \cdot \nabla(\frac{p_i}{\rho_i})$ component:

$$\mathbf{J}_i \cdot \nabla\left(\frac{p_i}{\rho_i}\right) = J_{z,i}\frac{\partial}{\partial z}\left(\frac{p_i}{\rho_i}\right) + J_{r,i}\frac{\partial}{\partial r}\left(\frac{p_i}{\rho_i}\right).$$

6. $[d_t\mathbf{u} \cdot (\mathbf{\Pi}_i + \omega f_b \Delta_i \mathbf{I})]$ components:

$$d_t\mathbf{u} \cdot (\mathbf{\Pi}_i + \omega f_b \Delta_i \mathbf{I})]_z = \Pi_{zz,i}\left(u\frac{\partial u}{\partial z} + v\frac{\partial u}{\partial r}\right) + \Pi_{rz,i}\left(u\frac{\partial v}{\partial z} + v\frac{\partial v}{\partial r}\right) + \omega f_b \Delta_i\left(u\frac{\partial u}{\partial z} + v\frac{\partial u}{\partial r}\right),$$
$$[d_t\mathbf{u} \cdot (\mathbf{\Pi}_i + \omega f_b \Delta_i \mathbf{I})]_r = \Pi_{rr,i}\left(u\frac{\partial v}{\partial z} + v\frac{\partial v}{\partial r}\right) + \Pi_{rz,i}\left(u\frac{\partial u}{\partial z} + v\frac{\partial u}{\partial r}\right) + \omega f_b \Delta_i\left(u\frac{\partial v}{\partial z} + v\frac{\partial v}{\partial r}\right).$$

7. $[\mathbf{Q}_i' \cdot \nabla u]$ components:

$$[\mathbf{Q}_i' \cdot \nabla u]_z = Q_{z,i}'\frac{\partial u}{\partial z} + Q_{r,i}'\frac{\partial u}{\partial r}, \quad [\mathbf{Q}_i' \cdot \nabla u]_r = Q_{z,i}'\frac{\partial v}{\partial z} + Q_{r,i}\frac{\partial v}{\partial r}.$$

8. $[\mathbf{\Pi}_i \cdot \mathbf{Q}_0']$ components:

$$[\mathbf{\Pi}_i \cdot \mathbf{Q}_0']_z = \Pi_{zz,i}Q_{0,z}' + \Pi_{rz,i}Q_{0,r}', \quad [\mathbf{\Pi}_i \cdot \mathbf{Q}_0']_r = \Pi_{rz,i}Q_{0,x}' + \Pi_{rr,i}Q_{0,y}'.$$

9. $\left[\nabla \cdot \left(\frac{p_i}{p}\mathbf{I} + \frac{\omega f_b}{Rep}\Delta_i\mathbf{I} + \frac{1}{Rep}\mathbf{\Pi}_i\right)\right]$ components:

$$\left[\nabla \cdot \left(\frac{p_i}{p}\mathbf{I} + \frac{\omega f_b}{Rep}\Delta_i\mathbf{I} + \frac{1}{Rep}\mathbf{\Pi}_i\right)\right]_z = \frac{1}{Rep}\left(\frac{\partial \Pi_{zz,i}}{\partial z} + \frac{\partial \Pi_{rz,i}}{\partial r} + \frac{\Pi_{rz,i}}{r}\right) + \frac{1}{p}\frac{\partial p_i}{\partial z} + \frac{\omega f_b}{Rep}\frac{\partial \Delta_i}{\partial z},$$
$$\left[\nabla \cdot \left(\frac{p_i}{p}\mathbf{I} + \frac{\omega f_b}{Rep}\Delta_i\mathbf{I} + \frac{1}{Rep}\mathbf{\Pi}_i\right)\right]_r = \frac{1}{Rep}\left(\frac{\partial \Pi_{rr,i}}{\partial r} + \frac{\partial \Pi_{rz,i}}{\partial z} + \frac{\Pi_{rr,i}}{r}\right) + \frac{1}{p}\frac{\partial p_i}{\partial r} + \frac{\omega f_b}{Rep}\frac{\partial \Delta_i}{\partial r}.$$

10. $[\nabla \cdot (\mathbf{\Pi} + \omega f_b \Delta \mathbf{I})]$ components:

$$[\nabla \cdot (\mathbf{\Pi} + \omega f_b \Delta \mathbf{I})]_z = \sum_j \left(\frac{\partial \Pi_{zz,j}}{\partial z} + \frac{\partial \Pi_{rz,j}}{\partial r} + \frac{\Pi_{rz,j}}{r} + \omega f_b \frac{\partial \Delta_j}{\partial z}\right),$$
$$[\nabla \cdot (\mathbf{\Pi} + \omega f_b \Delta \mathbf{I})]_r = \sum_j \left(\frac{\partial \Pi_{rr,j}}{\partial r} + \frac{\partial \Pi_{rz,j}}{\partial z} + \frac{\Pi_{rr,j}}{r} + \omega f_b \frac{\partial \Delta_j}{\partial r}\right).$$

11. $[\nabla \cdot (\mathbf{\Pi}_i + \omega f_b \Delta_i \mathbf{I})]$ components:

$$[\nabla \cdot (\mathbf{\Pi}_i + \omega f_b \Delta_i \mathbf{I})]_z = \frac{\partial \Pi_{zz,j}}{\partial z} + \frac{\partial \Pi_{rz,j}}{\partial r} + \frac{\Pi_{rz,j}}{r} + \omega f_b \frac{\partial \Delta_j}{\partial z},$$
$$[\nabla \cdot (\mathbf{\Pi}_i + \omega f_b \Delta_i \mathbf{I})]_r = \frac{\partial \Pi_{rr,j}}{\partial r} + \frac{\partial \Pi_{rz,j}}{\partial z} + \frac{\Pi_{rr,j}}{r} + \omega f_b \frac{\partial \Delta_j}{\partial r}.$$

12. $[\mathbf{J}_i \cdot \nabla u]$ components:

$$[\mathbf{J}_i \cdot \nabla u]_z = J_{z,i}\frac{\partial u}{\partial z} + J_{r,i}\frac{\partial u}{\partial r}, \quad [\mathbf{J}_i \cdot \nabla u]_r = J_{z,i}\frac{\partial v}{\partial z} + J_{r,i}\frac{\partial v}{\partial r}.$$

13. Components of κ:

$$\mathbf{\Pi}_i : \mathbf{\Pi}_j = \Pi_{zz,i}\Pi_{zz,j} + \Pi_{rr,i}\Pi_{rr,j} + 2\Pi_{rz,i}\Pi_{rz,j} + \Pi_{\theta\theta,i}\Pi_{\theta\theta,j},$$
$$\mathbf{Q}_i' \cdot \mathbf{Q}_j' = Q_{z,i}'Q_{z,j}' + Q_{r,i}'Q_{r,j}',$$
$$\Delta_0 = -f_b\mu\left(\frac{\partial u}{\partial z} + \frac{\partial u}{\partial r} + \frac{\partial v}{\partial z} + \frac{\partial v}{\partial r}\right), \quad \mathbf{d}_i = \nabla\left(\frac{n_i}{n}\right) = \frac{\mathcal{M}}{\mathcal{M}_i}\nabla\left(\frac{\rho_i}{\rho}\right),$$

where

$$\mathcal{M} = \sum_j \mathcal{M}_j\left(\frac{n_j}{n}\right), \quad [\mathbf{d}_i]_z = \frac{\mathcal{M}}{\mathcal{M}_i}\frac{\partial}{\partial z}\left(\frac{\rho_i}{\rho}\right), \quad [\mathbf{d}_i]_r = \frac{\mathcal{M}}{\mathcal{M}_i}\frac{\partial}{\partial r}\left(\frac{\rho_i}{\rho}\right).$$

References

[1] T.I. Gombosi, Gaskinetic Theory, Cambridge University Press, 1994.
[2] B.C. Eu, Kinetic Theory and Irreversible Thermo-dynamics, Wiley, New York, 1992.
[3] C. Park, Nonequilibrium Hypersonic Aerothermodynamics, Wiley, New York, 1990.
[4] M.S. Ivanov, P.V. Vashchenkovy, A.V. Kashkovsky, Numerical modeling of high altitude aerodynamics of reentry vehicles, in: Proceedings of the Ninth AIAA/ASME Joint Thermophysics and Heat Transfer Conference, San Francisco, CA, Paper AIAA 2006-3801, 2006.
[5] Y.A. Bondar, G.N. Markelov, S.F. Gimelshein, M.S. Ivanov, Numerical modeling of near-continuum flow over a wedge with real gas effects, J. Thermophys. Heat Transfer 20 (4) (2006) 699–709.
[6] G.A. Bird, Molecular Gas Dynamics and the Direct Simulation of Gas Flows, Oxford University Press, Oxford, 1994.
[7] R.S. Myong, A generalized hydrodynamic computational model for rarefied and microscale diatomic gas flows, J. Comput. Phys. 195 (2004) 655–676.
[8] B.C. Eu, Generalized Thermodynamics: The Thermodynamics of Irreversible Processes and Generalized Hydrodynamics, Kluwer Academic Publishers, Dordrecht, 2002.
[9] K. Xu, M. Mao, L. Tang, A multidimensional gas-kinetic BGK scheme for hypersonic viscous flow, J. Comput. Phys. 203 (2005) 405–421.
[10] W. Liao, L.-S. Luo, K. Xu, Gas-kinetic scheme for continuum and near-continuum hypersonic flows, J. Spacecraft Rockets 44 (6) (2007) 1232–1240.
[11] D. Burnett, The distribution of molecular velocities and the mean motion in a nonuniform gas, Proc. Lond. Math. Soc. 40 (1935) 382–435.
[12] B.C. Eu, Transport Coefficients of Fluids, Springer, Berlin, 2006.
[13] B.C. Eu, Y.G. Ohr, Thermodynamically consistent equation of state of hard sphere fluids, J. Chem. Phys. 118 (5) (2003) 2264–2269.
[14] B.C. Eu, Generalized hydrodynamics in the transient regime and irreversible thermodynamics, Philos. Trans. R. Soc. Lond. A 362 (2004) 1553–1565.
[15] R.S. Myong, A computational method for Eu's generalized hydrodynamic equations of rarefied and microscale gas dynamics, J. Comput. Phys. 168 (2001) 47–72.
[16] B.C. Eu, Y.G. Ohr, Generalized hydrodynamics, bulk viscosity, and sound wave absorption and dispersion in dilute rigid molecular gases, Phys. Fluids 13 (3) (2001) 744–753.
[17] S. Chapman, T.G. Cowling, The Mathematical Theory of Nonuniform Gases, Cambridge University Press, London, 1970.
[18] C.F. Curtiss, The classical Boltzmann equation of a gas of diatomic molecules, J. Chem. Phys. 75 (1) (1981) 376–378.
[19] G.V. Candler, The Computation of Weakly Ionized Hypersonic Flows in Thermo-Chemical Nonequilibrium, Ph.D. Thesis, Stanford University, 1988.
[20] J. Häuser, J. Muylaert, H. Wong, W. Berry, Computational Aerothermodynamics for 2D and 3D Space Vehicles, Computational Methods in Hypersonic Aerodynamics, Kluwer Academic Publishers, London, 1991.
[21] I. Langmuir, J. Am. Chem. Soc. 40 (1918) 1361.
[22] A.W. Adamson, Physical Chemistry of Surfaces, John Wiley and Sons, New York, 1982.
[23] R.S. Myong, J.M. Reese, R.W. Barber, D.R. Emerson, Velocity slip in microscale cylindrical Couette flow: the Langmuir model, Phys. Fluids 17 (2005) 087105.
[24] R.S. Myong, Velocity-slip effect in low-speed microscale gas flows, in: Proceedings of the 35th AIAA Thermophysics Conference, Aneheim, CA, Paper AIAA 2001-3076, 2001.
[25] A. Beskok, G.E. Karniadakis, Simulation of heat and momentum transfer in complex microgeometries, J. Thermophys. Heat Transfer 8 (4) (1994) 647–655.
[26] G.E. Karniadakis, A. Beskok, Micro Flows, Springer, New York, 2002.
[27] W.H. Press, B.P. Flannery, S.A. Teukolsky, W.T. Vetterling, Numerical Recipe in Fortran 77, Cambridge University Press, London, 1993.
[28] K.H. Kim, C. Kim, O. Rho, Methods for the accurate computations of hypersonic flows. 1: AUSMPW+ scheme, J. Comput. Phys. 174 (2001) 38–80.
[29] N.-T. Nguyen, S.T. Wereley, Fundamentals and Applications of Microfluidics, Artech House Inc., Norwood, MA, 2002.
[30] E.F. Greene, D.F. Hornig, The shape and thickness of shock fronts in argon, hydrogen, nitrogen and oxygen, J. Chem. Phys. 21 (4) (1953) 617–624.
[31] M. Linzer, D.F. Hornig, Structure of shock fronts in argon and nitrogen, Phys. Fluids 6 (12) (1963) 1661–1668.
[32] M. Camac, in: Proceedings of the Fourth International Symposium on Rarefied Gas Dynamics, vol. 1, 1965, p. 240.
[33] F. Robben, L. Talbot, Measurement of shock wave thickness by the electron beam fluorescence method, Phys. Fluids 9 (4) (1966) 633–643.
[34] H. Alsmyer, Density profiles in argon and nitrogen shock waves measured by the absorption of an electron beam, J. Fluid Mech. 74 (1976) 497–513.
[35] I.D. Boyd, G. Chen, G.V. Candler, Predicting failure of the continuum fluid equations in transitional hypersonic flows, Phys. Fluids 7 (1) (1995) 210–219.
[36] M. Al-Ghoul, B.C. Eu, Generalized hydrodynamic theory of shock waves: mach-number dependence of inverse shock width for nitrogen gas, Phys. Rev. Lett. 86 (19) (2001) 4294–4297.
[37] M. Al-Ghoul, B.C. Eu, Generalized hydrodynamic theory of shock waves in rigid diatomic gases, Phys. Rev. E 64 (2001) 046303.
[38] J.S. Wu, K.C. Tseng, C.H. Kuo, Application of local mesh refinement in the DSMC method, in: Rarefied Gas Dynamics: 22nd International Symposium, AIP Conference Proceedings, vol. 585, 2001, pp. 417–425.
[39] S. Chigullapalli, A. Venkattraman, A.A. Alexeenko, M.S. Ivanov, Non-equilibrium flow modeling using high-order schemes for the Boltzmann model equations, in: Proceedings of the 40th Thermophyics Conference, Seattle, Washington, Paper AIAA 2008-3929, 2008.
[40] G.F. Naterer, J.A. Camberos, Entropy and the second law fluid flow and heat transfer simulation, J. Thermophys. Heat Transfer 17 (3) (2003) 360–371.
[41] K.Y. Yun, R.K. Agarwal, R. Balakrishnan, Augmented Burnett and Bhatnagar–Gross–Burnett equations for hypersonic flow, J. Thermophys. Heat Transfer 12 (3) (1998) 328–335.
[42] J.N. Moss, G.A. Bird, Direct simulation of transitional flow for hypersonic reentry conditions, in: Proceedings of the 22nd AIAA Aerospace Science Meeting, Reno, NV, Paper AIAA 84-0223, 1984.
[43] V.K. Dogra, R.G. Wilmoth, J.N. Moss, Aerothermodynamics of a 16-meter-diameter sphere in hypersonic rarefied flow, AIAA J. 30 (7) (1992) 1789–1794.
[44] V.K. Dogra, J.C. Taylor, H.A. Hassan, Blunt body rarefied wakes for earth entry, J. Thermophys. Heat Transfer 9 (3) (1995) 464–470.
[45] R.N. Gupta, J.M. Yos, R.A. Thompson, K.P. Lee, A Review of Reaction Rates and Thermodynamic and Transport Properties for an 11-Species Air Model for Chemical and Thermal Nonequilibrium Calculations to 30,000K, NASA RP-1232, 1990.
[46] C.R. Wilke, A viscosity equation for gas mixtures, J. Chem. Phys. 18 (1950) 517.